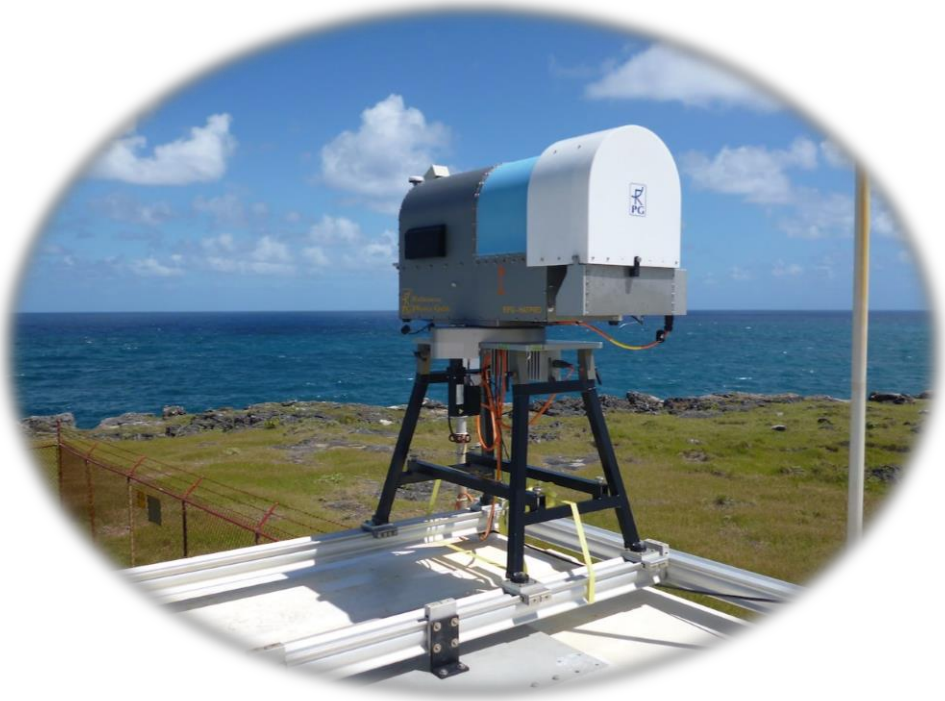

Exploitation of Ground-Based Water Vapour Radiometers in Satellite Altimetry

Bernard Costa Vasconcellos

Dissertação de Mestrado apresentada à
Faculdade de Ciências da Universidade do Porto em
Deteção Remota

2021

Orientadora
Maria Joana Fernandes, Professora Associada com Agregação
Faculdade de Ciências, Universidade do Porto
Porto, Portugal

Coorientadora
Maria Clara Lázaro da Silva, Professora Auxiliar
Faculdade de Ciências, Universidade do Porto
Porto, Portugal

Todas as correções determinadas pelo júri, e só essas, foram efetuadas.

O Presidente do Júri,

Porto, 21 / 12 / 2021

Abstract

Satellite altimetry has become a standard tool for many Earth Observation studies applied to sea, glaciers, rivers, inland waters and lakes, in order to measure the height of a water body above a reference ellipsoid. The signal emitted by the altimeter sensor is highly dependent on the wet tropospheric correction (WTC), due to the signal interaction with water vapour suspended in this atmospheric layer. Since water vapour does not behave as a well-mixed gas, its prediction becomes a delicate task. Therefore, microwave radiometers are on board the altimeter satellites in order to determine the WTC very accurately over open-ocean. Despite the ability of this passive sensor to produce collocated measurements with the altimeter, other sources of WTC are needed in locations where observations are invalidated due to the presence of non-ocean surfaces in its footprint, such as in coastal areas and high latitudes.

This study aims to investigate ground-based radiometers (MWR_{GB}) as a reliable source of water vapour measurements for deducing the WTC of altimetric observations. For this purpose, the WTC from the MWR_{GB} is assessed by comparison with other four external WTC sources: on-board microwave radiometers (MWR_{OB}), Global Navigation Satellite Systems (GNSS), Numerical Weather Models (NWM), and radiosonde (RS).

MWR_{GB} from three observatories of the Atmospheric Radiation Measurements (ARM) facility have been used in this study: ENA (Eastern North Atlantic), SGP (Southern Great Plains) and, OLI (Oliktok Point in Alaska). Among them, only for the ENA observatory it was possible to perform the assessment with all external sources while the OLI and SGP observatories produced results with only 2 sources. For OLI, comparisons were performed with MWR_{OB} and NWM, and for SGP with RS and NWM. In addition, retrievals from two ARM algorithms were used in order to evaluate which one best suits the needs of Satellite altimetry – NN or MWRRETV2.

For the ENA observatory, collocated comparisons and up to 40 km (MWR_{OB}, NWM and GNSS), showed RMS of WTC differences in the range 1.02 cm - 1.41 cm. For the comparison with RS, which is non-collocated at 89 km, an RMS of 2.37 cm was found. For the OLI observatory, the comparison with NWM presented an RMS in the range of 0.56 cm - 0.50 cm. In contrast, for the same observatory, the comparison with MWR_{OB} up to 40 km had an RMS from 1.84 cm to 2.53 cm, indicating the existence of MWR_{OB} observations contaminated by land or sea ice. For the SGP observatory, the collocated comparisons with NWM and RS had RMS in the range of 1.18 cm - 1.89 cm

The intra-algorithm assessment showed that in general the NN and MWRRETV2 algorithms have great similarity in their results, with a variation of RMS of WTC differences in the range of 0 – 7.0 mm. Therefore, for the needs of Satellite Altimetry up to 40 km, the NN algorithm proves to be a reliable source for deducing WTC_{GB}, due to the near real-time latency of its retrieved data.

At last, only for the ENA observatory, two neural network algorithms were tuned to estimate the WTC directly from MWR_{GB} brightness temperatures (TB) observations, which are: (WTC_{GB_2TB}) using 2 inputs - TB from both the 23.8 and 30 GHz bands; and (WTC_{GB_3TB}), using 3 inputs – the former two TB with further inclusion of the TB from the 90 GHz bands. An independent assessment for the WTC values retrieved from both algorithms was carried out with GNSS. WTC_{GB_2TB} presented an RMS of 1.42 cm while the WTC_{GB_3TB} obtained a better performance of 1.34 cm. Furthermore, the comparison with the NN algorithm, for the same period, showed an RMS of 1.41 cm, which was higher than the result found for the WTC_{GB_3TB}.

Resumo

A Altimetria por Satélite tornou-se uma ferramenta padrão para vários estudos de Observação da Terra aplicados ao mar, glaciares, rios, águas interiores e lagos, com o objetivo de medir a altura do corpo de água acima de uma elipsoide de referência. O sinal emitido pelo sensor do altímetro é altamente dependente da correção troposférica devido à componente húmida (*Wet Tropospheris Correction*, WTC), causada pela interação do sinal com vapor de água suspenso nesta camada da atmosfera. Uma vez que o vapor de água não se comporta como um gás bem misturado, a sua previsão torna-se uma tarefa delicada. Portanto, radiómetros de micro-ondas estão a bordo dos satélites a fim de determinar a WTC com grande precisão sobre o oceano. Apesar da capacidade deste sensor passivo em produzir medições colocadas com o altímetro, outras fontes da WTC são necessárias em locais onde as observações são invalidadas devido à presença de terra e gelo na sua pegada, tais como em zonas costeiras e latitudes elevadas.

Este estudo visa investigar radiómetros terrestres (MWR_{GB}) como uma fonte precisa da WTC a partir das medições de vapor de água. Para esse fim, o WTC do MWR_{GB} é avaliado por comparação com outras quatro fontes externas de WTC: radiómetros de microondas a bordo das missões altimétricas (MWR_{OB}), *Global Navigation Satellite Systems* (GNSS), *Numerical Weather Models* (NWM) e Radiosondas (RS).

Neste estudo foram utilizados MWR_{GB} de três observatórios do ARM (T*he Atmospheric Radiation Measurement user facility*): ENA (*Eastern North Atlantic*), SGP (*Southern Great Plains*) e OLI (*Oliktok Point in Alaska*). Entre estes, apenas para o observatório ENA foi possível realizar a avaliação com todas as fontes externas, enquanto os observatórios OLI e SGP produziram resultados com apenas 2 fontes. Para o observatório OLI foram efetuadas comparações com MWR_{OB} e NWM; e para o SGP com RS e NWM. Além disto, foram utilizados dados de WTC_{GB} estimados de dois algoritmos do ARM, com o objetivo de avaliar qual deles melhor se adequa às necessidades da altimetria por satélite - NN ou MWRRETV2.

Para o observatório ENA, as comparações colocadas e até 40 km (MWR_{OB}, NWM e GNSS), apresentaram valores de RMS no intervalo de 1,02 cm - 1,41 cm, enquanto a comparação com RS, que foi não colocada em 89 km, obteve um RMS de 2,37 cm. Para o observatório OLI, a comparação com NWM apresentou um RMS no intervalo de 0,50 cm - 0,56 cm. Em contraste, para o mesmo observatório, a comparação com MWR_{OB} até 40 km de distância obteve um RMS de 1,84 cm a 2,53 cm, indicando a existência de observações do MWR_{OB} contaminadas por gelo ou terra. Para o observatório do SGP, as comparações com NWM e RS apresentaram valores de RMS na faixa de 1,18 cm - 1,89 cm.

A avaliação entre os algoritmos NN e MWRRETV2 demonstrou que ambos possuem grande semelhança nos seus resultados, com uma variação de RMS na gama de 0 - 7,0 mm. Portanto, para as necessidades de Altimetria de Satélite até 40 km, o algoritmo NN revela-se uma fonte fiável para deduzir a WTC, devido à latência quase em tempo real dos seus dados recuperados.

Por fim, apenas para o observatório ENA, dois algoritmos de rede neural foram treinados para estimar o WTC diretamente a partir das observações de temperaturas de brilho (TB) do MWR_{GB}, que são: ($WTC_{GB}\_2_{TB}$), utilizando 2 inputs - TB das bandas de 23,8 e 30 GHz; e ($WTC_{GB}\_3_{TB}$), utilizando 3 inputs - as duas primeiras TB com inclusão adicional da TB da banda de 90 GHz. Foi realizada, por fim, uma avaliação independente dos valores do WTC obtidos a partir de ambos algoritmos contra GNSS. Os resultados mostraram que o $WTC_{GB}\_2_{TB}$ obteve um RMS de 1,42 cm enquanto o $WTC_{GB}\_3T_B$ obteve um melhor desempenho, de 1,34 cm. Além disto, a comparação com o algoritmo NN, para o mesmo período, mostrou um RMS de 1,41 cm, superior ao resultado encontrado para o $WTC_{GB}\_3_{TB}$.

Acknowledgements

I would like to dedicate this space to thank the people who had a direct participation in this work.

First of all, to professors Joana Fernandes and Clara Lázaro for believing in my potential and giving me the best opportunity I have ever had in my life. After this last year on the Satellite Altimetry group, I feel very privileged to have learned so much from two strong women in science.

To Professor Joana specifically, my most sincere thanks for all her patience, attention, kindness, and willingness to show me the best paths to follow.

To Telmo Vieira, for always being open to share his knowledge on a daily basis.

To my family on the other side of the ocean, my parents João and Elizabete, for always having stimulated me to enjoy studying in the most diverse ways and also for giving me support in difficult decisions.

Finally, to my girlfriend Carolina Andriola, for all the emotional support and companionship.

List of Acronyms

ARM	Atmospheric Radiation Measurement user facility
NetCDF	Network Common Data Form
CSV	Comma-Separated Values
ECMWF	European Centre for Medium-Range Weather Forecasts
ENA	Eastern North Atlantic - ARM
ENAO	Eastern North Atlantic Observatory IGS
EO	Earth Observation
EPA	U.S. Environmental Protection Agency
ERA5	ECMWF Reanalysis v5
EUMETSAT	European Organisation for the Exploitation of Meteorological Satellites
GNSS	Global Navigation Satellite Systems
GPT	Global Pressure and Temperature model
GVR	G-Band Vapor Radiometer
GVRP	G-band Vapor Radiometer Profiler
HRES	Atmospheric Model High Resolution 10-day forecast
IGRA	Integrated Global Radiosonde Archive
IGS	International GNSS Service
LWP	Liquid Water Path
MJD	Modified Julian Date
MWR	Microwave Radiometer
MWR3C	Microwave Radiometer 3-Channel
MWR$_{GB}$	Ground-Based Microwave Radiometer
MWR$_{OB}$	Microwave Radiometer On Board Satellites
MWRHF	Microwave Radiometer-High Frequency
MWRRET	Microwave Radiometer Retrieval
MWRRETV2	Microwave Radiometer Retrieval Version 2
NCEP	National Centers for Environmental Prediction
NN	Neural Network

NOAA	National Oceanic and Atmospheric Administration
NSA	North Slope of Alaska
NWM	Numerical Weather Models
OLI	Oliktok Point, Alaska
PD	Path Delay
RADS	Radar Altimeter Database System
RMS	Root Mean Square Error
RS	Radiosonde
SGP	Southern Great Plains
SLA	Sea Level Anomaly
SSH	Sea Surface Height
STD	Slant Total Delay
TB	Brightness Temperatures
TCWV	Total Column Water Vapour
U.S.	United States of America
WTC	Wet Tropospheric Correction
WTC_{GB}	Wet Tropospheric Correction from Ground-Based Microwave Radiometer
$WTCG_{NWM}$	Wet Tropospheric Correction from Numerical Weather Models
WTC_{GNSS}	Wet Tropospheric Correction from Global Navigation Satellite Systems
WTC_{OB}	Wet Tropospheric Correction from Microwave Radiometer On Board Satellites
WTC_{RS}	Wet Tropospheric Correction from Radiosonde
ZHD	Zenith Hydrostatic Delay
ZTD	Zenith Total Delay
ZWD	Zenith Wet Delay

Contents

ABSTRACT ..... **I**

ACKNOWLEDGEMENTS ..... **III**

LIST OF ACRONYMS ..... **IV**

LIST OF FIGURES ..... **VII**

1. INTRODUCTION **1**

1.1 THESIS OBJECTIVES 4

1.2 THESIS OUTLINE 5

2. WTC SOURCES FOR SATELLITE ALTIMETRY **6**

2.1 GROUND-BASED MICROWAVE RADIOMETERS 6

2.2 GLOBAL NAVIGATION SATELLITE SYSTEMS 11

2.3 ON-BOARD MICROWAVE RADIOMETERS 14

2.4 NUMERICAL WEATHER MODELS 16

2.5 RADIOSONDES 18

3. DATA DESCRIPTION **20**

3.1 GROUND-BASED RADIOMETER DATA FROM ARM 22

3.2 WET TROPOSPHERIC CORRECTION FROM GNSS 24

3.3 WET TROPOSPHERIC CORRECTION FROM ON-BOARD MWR 24

3.4 WET TROPOSPHERIC CORRECTION FROM ERA5 25

3.5 RADIOSONDE DATA FROM IGRA 26

4. ASSESSMENT OF THE WTC FROM GROUND-BASED RADIOMETERS **27**

4.1 METHODOLOGICAL APPROACH 27

4.2 COMPARISON WITH NUMERICAL WEATHER MODEL 29

4.3 COMPARISON WITH ON-BOARD MICROWAVE RADIOMETERS 34

4.4 COMPARISON WITH RADIOSONDES 42

4.5 COMPARISON WITH GNSS 45

5. CONCLUSION **48**

6. REFERENCES **51**

List of Figures

Figure 1 - First MWR_{GB} prototype, Mark-I Radiometric Thermasonde. Figure retrieved from [25]. ... 6

Figure 2 – Attenuation profile of the atmosphere due to water vapour and oxygen. Figure modified from [16]. ... 7

Figure 3 – Example of Attenuation profiles of the atmosphere for different densities of water vapour and liquid water. Figure retrieved from [24]. ... 8

Figure 4 - Geographical representations of the ARM Observatories. Green represents fixed observatories while blue represents mobile observatories that are currently in operation or otherwise. Figure modified from [38]. ... 10

Figure 5 - Representation of the ZTD determination, for a GNSS station, from several STD products for a given time. Figure modified from [46]. ... 12

Figure 6 - Geographical locations of GNSS stations belonging to the IGS network in August 2021 [50]. ... 12

Figure 7 – Amplitude of the annual component of WTC_{NWM} (in cm), computed from the TCWV field of ERA5 *single-level parameters*. The location of the ARM observatories is represented in violet points. Figure modified from [15]. ... 17

Figure 8 - Geographical locations of radiosondes launch sites belonging to the IGRA network in August 2021 [70]. ... 19

Figure 9 – Spatial distribution of the WTC sources around the ENA observatory – Azores, Portugal. Top figure: MWR_{GB} (ENA), GNSS, radiosonde, Jason-3, Sentinel-3 A and B. Bottom right figure: MWR_{GB} (ENA), SARAL/AltiKa. Bottom left figure: WTC source labels. ... 20

Figure 10 - Spatial distribution of the WTC sources around the OLI observatory – Alaska, U.S. Top figure: MWR_{GB} (OLI) and Sentinel-3 A and B. Bottom figure: MWR_{GB} (ENA), SARAL/AltiKa. For this figure, the WTC source labels are the same as for Figure 9..... 21

Figure 11 - Spatial distribution of the WTC sources around the SGP observatory – Oklahoma, U.S.: MWR_{GB} (SGP) and radiosonde. For this figure, the WTC source labels are the same as for Figure 9. 22

Figure 12 - Complete time series of the observatories ENA (top), OLI (centre) and SGP (bottom). The graphs are WTC_{GB} values deduced from the NN (in blue) and MWRRETV2 (in red) algorithms where points with a darker shade of blue are measurements overlapped between algorithms. 23

Figure 13 - Mean (top) and StD (bottom) of WTC_{NWM} (in cm), computed from the TCWV field of ERA5 *single-level parameters* over a period of one year. The location of the ARM observatories is represented in violet points. 25

Figure 14 - RMS of the daily WTC differences between the products of the ARM algorithms and the ERA5 climate model, for the ENA observatory. 30

Figure 15 - RMS of the daily WTC differences between the products of the ARM algorithms and the ERA5 climate model, for the OLI observatory. 31

Figure 16 - RMS of the daily WTC differences between the products of the ARM algorithms and the ERA5 climate model, for the SGP observatory..... 32

Figure 17 - RMS of the WTC differences between the products of the ARM algorithms and the Sentinel 3A on-board MWR, for the ENA observatory. The differences were computed for 5 classes of distance to the ENA Observatory. 34

Figure 18 - RMS of the WTC differences between the products of the ARM algorithms and the Sentinel 3B on-board MWR, for the ENA observatory. The differences were performed for 5 classes of distance to the ENA Observatory. 35

Figure 19 - RMS of the WTC differences between the products of the ARM algorithms and the SARAL/AltiKa on-board MWR, for the ENA observatory. The differences were performed for 5 classes of distance to the ENA Observatory. 36

Figure 20 - RMS of the WTC differences between the products of the ARM algorithms and the Jason-3 on-board MWR, for the ENA observatory. The differences were performed for 2 classes of distance to the ENA Observatory. 37

Figure 21 - RMS of the WTC differences between the products of the ARM algorithms and the Sentinel 3A on-board MWR, for the OLI observatory. The differences were computed for 4 classes of distance to the OLI Observatory. 38

Figure 22 - RMS of the WTC differences between the products of the ARM algorithms and the Sentinel 3B on-board MWR, for the OLI observatory. The differences were performed for 4 classes of distance to the OLI Observatory. 39

Figure 23 - RMS of the WTC differences between the products of the ARM algorithms and the SARAL on-board MWR, for the OLI observatory. The differences were performed for 5 classes of distance to the OLI Observatory..... 40

Figure 24 - WTC differences between the products of the radiosonde and ARM algorithms for the ENA observatory - NN (top) and MWRRETV2 (bottom)..... 43

Figure 25 - WTC differences between the products of the ARM and radiosonde algorithms for the SGP observatory - NN (top) and MWRRETV2 (bottom). 44

Figure 26 - RMS of the WTC difference of NN, WTC_{GB_2TB} and, WTC_{GB_3TB} algorithms relative to the GNSS data, for the ENA observatory. The data period collected is approximately 15 consecutive months..... 46

List of Tables

Table 1 - Types of MWR_{GB} developed by the ARM with channel descriptions and retrieval parameters. Table adapted from [33] 9

Table 2 - Description of the on-board microwave radiometer channels that are utilised by current altimetry missions. Table includes the launch year of each mission. 15

Table 3 - Geographic locations of the observatories ENA, OLI and SGP. Latitude and longitude are in decimal degrees and Height is above mean sea level. 22

Table 4 – Details of ENAO – IGS GNSS station. Table includes Latitude and longitude in decimal degrees and Height above geoid (orthometric height). 24

Table 5 - List of altimetric missions used in the comparison with MWR_{OB} for the OLI and ENA observatories. 25

Table 6 - Interpolated Mean (absolute values) and StD values of WTC_{NWM} along one year for the ENA, OLI and, SGP observatories. 26

Table 7 - List of RS stations used in the comparisons (WTC_{GB}, WTC_{RS}) for ENA and SGP observatories. Table includes Latitude and longitude in decimal degrees and Height above geoid (orthometric height). 26

Table 8 – Global statistics of the WTC differences between the products of the ARM algorithms and the ERA5 climate model, for the ENA observatory. 30

Table 9 – Global statistics of the WTC differences between the products of the ARM algorithms and the ERA5 climate model, for the OLI observatory. 31

Table 10 – Global statistics of the WTC differences between the products of the ARM algorithms and the ERA5 climate model, for the SGP observatory. 32

Table 11 - Number of samples, per class, which is the same for both NN and MWRRETV2 algorithm assessment. This table refers to the results shown in Figure 17. 34

Table 12 – Number of samples, per class, which is the same for both NN and MWRRETV2 algorithm assessments. This table refers to the results shown in Figure 18. 35

Table 13 - Number of samples, per class, which is the same for both NN and MWRRETV2 algorithm assessments. This table refers to the results shown in Figure 19. 36

Table 14 – Number of samples, per class, which is the same for both NN and MWRRETV2 algorithm assessments. This table refers to the results shown in Figure 20. 37

Table 15 – Number of samples, per class, which is the same for both NN and MWRRETV2 algorithm assessments. This table refers to the results shown in Figure 21. 38

Table 16 – Number of samples, per class, which is the same for both NN and MWRRETV2 algorithm assessments. This table refers to the results shown in Figure 22. 39

Table 17 – Number of samples, per class, which is the same for both NN and MWRRETV2 algorithm assessments. This table refers to the results shown in Figure 23. 40

Table 18 - Global statistics of the WTC difference between the products of the ARM algorithms and the radiosonde, for the ENA observatory. 43

Table 19 – Global statistics of the WTC differences between the products of the ARM algorithms and the radiosonde, for the SGP observatory. 45

Table 20 – Global statistics parameters of the WTC differences of NN, WTC_{GB_2TB} and, WTC_{GB_3TB} algorithms relative to the GNSS data, for the ENA observatory. 46

1. Introduction

Earth Observation (EO), by means of spacecraft sensors, has been largely used to monitor and record various surface types at different spatial, temporal, and spectral resolutions. The observation is through the detection of different bands of the electromagnetic spectrum [1] and can be done by either an active or passive sensor. The former detects the return of its own energy backscattered by the surface while the latter detects the energy emitted or reflected by a surface. In general, the retrieved data from the observations are georeferenced images or pointwise measurements. These enable multidisciplinary applications for understanding distinctive areas related to Earth dynamics, such as geodetic, meteorological, environmental and oceanographic studies. Satellite Altimetry is one of the EO techniques which, in the last 28 years, has allowed the determination of essential parameters such as the sea surface height (SSH), sea level anomaly (SLA), significant wave height, backscattering coefficient (sigma0) and wind speed. These are then utilised for ocean forecasting systems and climate monitoring applications [2].

TOPEX/Poseidon (T/P) was the first satellite fully designed to be a reference altimetry mission by the efforts of the *National Aeronautics and Space Administration* (NASA) and the *Centre National d'Études Spatiales* (CNES) [3]. Since T/P launch in 1992, Satellite Altimetry has become a standard tool for several EO studies applied to the sea, glaciers and inland waters (namely rivers, lakes and reservoirs) for the purpose to measure the height of the water body above a reference ellipsoid [2,4]. Due to T/P accomplishment, a cross-validation of the data from altimeters on board other non-exclusive altimetry missions, e.g., ERS-1 (1991-2000), ERS-2 (1995-2001) and Envisat (2002-2011) was achievable. This allowed a high temporal and spatial resolution through the merging of multi satellite datasets at a global scale, as shown in [5]. These authors found excellent compatibility by merging the T/P and ERS-1/2 altimeter datasets, achieving RMS (Root Mean Square Error) errors of their SLA differences of less than 2 or 3 cm in regions of low ocean variability. Nowadays, the foregoing missions are out of operation, but were important for the improvement of the technology that has been used in the various follow on missions. The following altimeter missions are currently operating: Cryosat-2 (2010-present), SARAL (2013-present), Jason-3 (2016-present), Sentinel-3 A and B (2016-present; 2018-present) and Sentinel-6 (2020-present). Accordingly, they grant a state-of-the-art water height overall accuracy of 1 to 3 cm [6].

The radar altimeter instrument carried on board the satellites is an active sensor that emits a pulse of microwave radiation within the range of 3.2 - 35 GHz [7]. The energy pulse is emitted, point by point towards the water surface, and the time (t) taken by the echo to return to the spacecraft is recorded by the altimeter [8]. Inserting the measured parameter t in Equation (1), the distance between the sensor and the water surface, nominally referred as range (R), is obtained.

$$R = \frac{c.t}{2} \tag{1}$$

In Equation (1): R = range (m); c = speed of light ($m.s^{-1}$); t = echo return time (s).

Furthermore, due to the capacity to determine the spacecraft's orbit in the order of 1 cm radial accuracy [9], the distance between the reference ellipsoid and the altimeter (H) is a known measure. Thus, the height of the water body (SSH) above the same ellipsoid is obtained by means of Equation (2):

$$SSH = \mathrm{H} - \mathrm{R} \quad (2)$$

However, Equation (1) considers that the electromagnetic energy at microwave frequencies propagates in free space, omitting the signal path delay (PD). The PD is induced by suspended molecules present in the atmosphere in three fundamental states of matter: liquid and gas (Troposphere) and plasma (Ionosphere). In other words, the signal entering into the atmosphere travels slower than the speed of light, due to the interaction - namely refraction - of the microwave signal with various atmospheric components. Thus, the reception of the echo by the altimeter is delayed, resulting in a measured R greater than the actual range.

Following this approach, altimeter range corrections are then indeed necessary to have reliable sea surface height (SSH) values [3] and various works have been carried out aiming to get more accurate measurements [10 - 15]. The range corrections are: (1) the *wet tropospheric correction* (WTC), accounting for the PD caused by the presence of water in the troposphere, both in liquid and vapour states [10,12,13]; (2) the *dry tropospheric correction* (DTC), due to the PD induced by the dry constituents of the troposphere - Nitrogen, Oxygen and Argon [15]; (3) the *ionospheric correction* (IC), caused by the free electrons content in the ionosphere which varies depending mainly on the solar activity period [11]; and (4) the *sea state bias* (SSB) which refers to an error in the altimeter range measurement and is originated by the existence of waves on the ocean surface [14]. Although all these corrections can be estimated through algorithms, forecasting models, instruments, and measurement techniques, the WTC is the range correction with the largest source of uncertainty nowadays [2,10], with mean values ranging from 0 to 35 cm [7]. This uncertainty is explained due to the high temporal and spatial variability of water vapour in the troposphere [15].

The water vapour is the most essential of the green-house gases that maintain the Earth warmed enough to sustain life. For example, the warming effect of this gas alone, compared to all greenhouse gases, is around 36 - 66% and around 66 - 85% when considering the clouds [16]. The horizontal variability of water vapour was addressed in [15], by means of WTC data over the ocean from January 1, 1988 - December 31, 2015. The authors found that the WTC variability is highly latitude-dependent, and in general terms, the WTC is higher in absolute values close to the equator with the largest variance near the tropics. In addition, lower absolute values and variances were reported as the distance to the poles decreases. This result is in agreement with Karmakar in [16], which presented the Clausius-Clapeyron relation that associates the air's capacity to retain more water vapour with the temperature increase. Besides the characteristic that water vapour has a high variation in the troposphere, this molecular state also does not behave as a well-mixed gas which makes predicting its content with a high degree of accuracy a challenging task [16].

To overcome this need, most altimetry missions are designed to deduce the WTC at the same instant of the altimeter sample by using a Microwave Radiometer on board (MWR$_{OB}$) the satellite. MWR$_{OB}$ is a passive sensor capable to retrieve the WTC (WTC$_{OB}$) with an accuracy of nearly 1 cm and *"[…] have been successfully used to monitor the temporal and spatial variations of sea surface and atmospheric properties on a global scale since the launch of the Soviet Cosmos-243 instrument in 1969."* [10]. The algorithms for retrieving the WTC$_{OB}$ from MWR$_{OB}$ measurements use the brightness temperatures (TB) detected by the instrument in its several channels [2]. Each channel detects the measured radiation in specific bands of the electromagnetic spectrum, where the joint rates of water vapour, liquid water and oxygen absorptions

contribute to the radiation attenuation. Thus, the TB are parameters that represent the energy received by the sensor antenna and are dependent on four geophysical properties: the atmospheric temperature, the atmospheric absorption profiles (of oxygen, water vapour and liquid water), the surface temperature, and the surface emissivity [10].

Despite the relevance of MWR$_{OB}$, there are some limitations in the corresponding WTC retrieval algorithms. These limitations are due to the fact that the algorithms are tuned to retrieve WTC under open ocean conditions, for which surface emissivity can be considered constant. One example of these limitations is using TB retrieved from observations in which the MWR$_{OB}$ footprint was contaminated from land, wetlands, and ice surface [2]. The algorithm then generates invalid measurements, which are identified and flagged.

Therefore, taking into account the large footprint of MWR$_{OB}$ (diameter with 8 – 43.4 km, varying with the frequency and instrument in usage, and the altitude of the spacecraft) [17,18], the determination of WTC is impaired in surface transition regions. This is explained due to the fact that the altimeter, which has a footprint (~ 3 km) well below the radiometer footprint [17], is still collecting information in these regions such as in coastal areas and inland waters.

Other methodologies have been used in order to obtain more accurate WTC values for these regions, such as the tropospheric delays provided by the Global Navigation Satellite System (GNSS) [2,6,13]. As in the altimeter range measurement, the signal emitted by GNSS satellites is delayed by the wet and dry gases present in the troposphere. The delay in the zenith direction is nominally referred as zenith total delay (ZTD). The ZTD at the station location, can be defined as the contribution of approximately 90% of the zenith hydrostatic delay (ZHD), a symmetrical value of the DTC; and of approximately 10% of the zenith wet delay (ZWD), a symmetrical value of the WTC (WTC$_{GNSS}$) [13]. In spite of the excellent accuracy in determining the ZWD by GNSS in order of mm, the system has not a spatial distribution suitable for a global coverage [15,19]. Hence, the accuracy of ZWD is lost as the satellite lies a few tens of kilometres from the GNSS station when compared to the collocated measurements without contamination made by MWR$_{OB}$ [6].

Another alternative to obtain reliable SSH values in these regions, or in case of missions without a MWR$_{OB}$ (e.g., Cryosat-2), is the utilization of numerical weather models (NWM) such as from the European Centre for Medium-Range Weather Forecasts (ECMWF). On the other hand, this methodology has been used to predict the WTC (WTC$_{NWM}$) with an accuracy lower than the collocated MWR$_{OB}$ measurements [7]. Thus, this should be used only when there are no other WTC sources available, e.g., WTC$_{GNSS}$ and WTC$_{OB}$ [4]. NWM are tabulated global values available in grids, e.g., 0.125°x0.125°, 0.75°x0.75°, and 0.25°x0.25°, in different temporal resolutions, e.g., 6 and 3 hours. One of the retrieved parameters used for deducing the WTC is the integrated water vapour profile, which can be referred as the Total Column Water Vapour (TCWV), or Precipitable Water (PW), or Integrated Water Vapour (IWV). The parameter is determined in each grid node, so spatial and temporal interpolations must be performed to select the corresponding TCWV for each altimeter sample. Consequently, NWM cannot modulate the high spatial variation of water vapour which reduces the accurate deduction of the WTC from NWM.

○ *Thesis Motivation*

Considering the findings of a more apparent trend of the increased water vapour content in the atmosphere in recent years on a global scale [20], followed by the also increasing trend of the WTC over

oceans [15], the concern to detect the water vapour content and distribution by the scientific community is evidenced. Therefore, non-space borne sensors such as the laser radar, microwave radiometer and radiosonde (RS) have been deployed across the globe in the past decades by meteorological monitoring systems. RS produces the principal parameters for atmospheric observations such as the water vapour profile, temperature, pressure, wind speed and TCWV [21]. As in the MWM, the TCWV measured by RS can be used to deduct the WTC (WTC_{RS}). This meteorological instrument consists in a set of atmospheric devices that are transported by a weather balloon along a vertical ascent from the ground, collecting information during its passage through the atmosphere. In addition, their observations of atmospheric water vapour profiles are used for the purpose of calibrating altimetry reference missions [2]. As it was shown in [17], databases of radiosonde measurements for different locations were used to train the T/P microwave radiometer retrieval algorithm.

Unfortunately, high costs and considerable effort is required to implement RS, their samplings are poorly distributed over time [21] (every 6 or 12 hours), resulting in a low spatial and temporal resolution. Thus, other technologies such as the Ground-Based Microwave Radiometer (MWR_{GB}) appear as an alternative to achieve better temporal resolution. MWR_{GB} enables continuous and autonomous measurements of the atmosphere such as the liquid water content, missing in radiosondes observations, and TCWV [21]. Although the latter parameter has a lower vertical resolution, in comparison with radiosondes, its determination has a commensurate accuracy [22]. In [23], a non-collocated comparison was carried out, at a distance of 37 km, between the two sensor datasets over a 15-years period. The authors concluded the existence of a total RMS error in the TCWV retrieved from MWR_{GB} of 1.9 mm. This is equivalent to a total RMS error in the WTC of approximately 12 mm (considering a WTC/TCWV ratio of 6.48 for TCWV = 1 mm and 5.97 for TCWV = 6 mm) [12].

In the scope of this dissertation, the proposal is to investigate the WTC retrieved from TCWV products of the MWR_{GB} measurements (WTC_{GB}). The motivation for this study rises from the fact that MWR_{GB} is an upward looking instrument and, conversely to MWR_{OB}, does not have the terrestrial surface as an interference in its measurements, but rather the cosmic space as a background. The space emissivity, therefore, has a constant contribution on TB values for all observations made by MWR_{GB} [16]. Furthermore, at the date of this dissertation, the use of MWR_{GB} measurements has not yet been exploited by satellite altimetry with the aim to contribute to the determination of more accurate WTC values in regions where the MWR_{OB} measurements are invalid.

1.1 *Thesis Objectives*

The aim of this study is to exploit the MWR_{GB} measurements as a WTC source for Satellite Altimetry observations. For this purpose, the following comparisons will be carried out in three different regions of the globe (Azores – Portugal, Alaska - U.S., and Oklahoma – U.S.).

The WTC_{GB} is assessed by comparison with other external WTC sources: MWR_{OB}, GNSS, RS and NWM. For each case, WTC differences, defined as the difference between the WTC from an external source (WTC_{OB}, WTC_{GNSS}, WTC_{RS} and WTC_{NWM}), when available, and the temporally corresponding WTC_{GB} are analysed. The first three comparisons can be collocated or not while the latter is collocated through spatial and temporal interpolation. Among all the comparisons, the only one that is not independent is the

comparison with radiosonde, since the information provided by this source is also introduced in the radiometer retrieval algorithms.

In regard to the behaviour of the wet component of the troposphere in three distinct locations, the expectation of this assessment is to understand the capability of this instrument in deducing the WTC. The ultimate goal is an evaluation of how the effect of the non-collocation, due to the distance between the MWR_{GB} and MWR_{OB}, affects the stability of these data as an accurate correction.

Additionally, two neural network algorithms have been trained in order to estimate the WTC directly from MWR_{GB} brightness temperature (TB) observations. With this algorithm, it is expected to suppress the errors associated to the known steps of deducing the WTC from the TCWV data, which are: (1) the previous estimation of TCWV values from TB using algorithms; and (2) the conversion of TCWV to WTC_{GB} using empirical expressions.

1.2 *Thesis Outline*

In addition to this present section, the Thesis has five further sections. The next section, 2., presents the background of the concepts employed in this study, as well as the various sources of the WTC data used and their acquisition. Section 3. briefly covers the specificities of the data collected for this study. Section 4. presents the implemented methodology and statistical analysis, as well as the results and discussions of the comparisons performed between the MWR_{GB} and the external sources. Section 5. presents the conclusions drawn regarding the whole context of this study. Lastly, section 6. gathers all the reference documents used in this thesis.

2. WTC Sources for Satellite Altimetry

This section aims to describe the various sources of WTC used in this study. As the objective of the work is to explore the use of MWRGB observations in Satellite Altimetry, the state-of-the.-art for this equipment is available in the first section (2.1). For the other WTC sources, such as GNSS (2.2), MWROB (2.3), NWM (2.4), and RS (2.5), the main concepts under study have been presented. At the end of each subsection the approaches adopted to obtain the WTC from each source are indicated.

2.1 *Ground-Based Microwave Radiometers*

Radiometric technology has played an important role in the in-depth understanding of the radiation transfer model at microwave frequencies - from the development of theory and its use in laboratory tests. One of the radiometry techniques is, for example, the measurement of atmospheric thermal emissions which is useful for various applications such as climate, geodesy, and validation [24]. In addition, continuous and autonomous measurements of the atmosphere in almost any weather condition are enabled when the technology is well designed in MWRGB [21]. At certain rain intensity level, MWRGB measurements are contaminated, generating corrupted data.

The ground-based microwave radiometer (MWRGB) sensing principle lies in being a passive receiver of the radiant flux that is emitted from the atmosphere plus the cosmic background radiation (~ 2.8 K). The radiance measured by the antenna sensor is then converted into TB, for each channel, using radiative transfer equations [16,21,22,24]. The input of these TB into algorithms allows the retrieval of several parameters of the atmosphere such as the temperature, integrated cloud liquid profile (nominally referred as LWP – liquid water path), and TCWV. Furthermore, these parameters are not easily determined accurately by other means [22], which make the radiometer even more relevant for climate issues.

During early uses of MWRGB, field experiments were aimed at determining the temperature profile of the atmosphere [25,26]. In 1965, the *U.S. Environmental Protection Agency* (EPA) contracted the *Sperry Corporation* to investigate the ability to use radiometry from the ground for this end. In the following years, an MWRGB prototype (Figure 1), Mark-I Radiometric Thermasonde, was developed and several measurement campaigns were organized to test the new equipment for different locations in the U.S. After the test period, assessments were conducted, for the collected data, in comparison with radiosondes, instrumented helicopters, and towers. This revealed new considerations about the measurements, and modifications were made in the Mark-I which was then delivered to EPA. Subsequently, EPA continued the studies aiming to collect temperature profile measurements for some specific locations. This phase took into consideration the need to perform data collection for

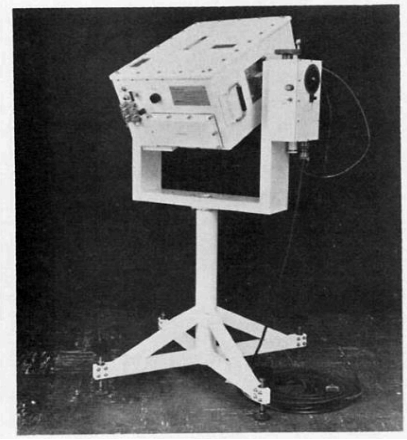

Figure 1 - First MWRGB prototype, Mark-I Radiometric Thermasonde. Figure retrieved from [25].

all environmental conditions. Finally, an improvement was made to the Mark-I to increase the equipment sensitivity [25].

○ *MWR$_{GB}$ Principles*

Due to Mark-I being designed for the determination of profile temperatures, the receiver was tuned to the frequency of 54.5 GHz, which is close to the maximum absorption peak band of suspended oxygen (O_2) molecules (Figure 2). The attenuation of the atmosphere caused by O_2 is due to the magnetic dipole transitions of the molecule that interact with electromagnetic radiations. These transitions lead to an absorption peak band in the 118.75 GHz and a complex band in between 50 and 70 GHz with the absorption peak at 61.151 GHz [16,28]. Hence, the intensity sensing by MWR$_{GB}$ in the O_2 complex range, on a cloudless day, can be interpreted as atmosphere temperature alone, since the water vapour attenuation contributes less in this frequency band [28]. During cloudy days, on the other hand, molecules of water vapour and especially of cloud liquid, which are suspended in the atmosphere, contaminate the temperature measurements. Thus, their proper correction requires such measurements to be made at frequencies outside the oxygen band, which infer liquid water and water vapour emissions, in order to obtain accurate temperature profiles [26]. Obtaining the air temperature profile then depends on the TB measured by the sensor, and therefore, statistical inversion techniques were developed for this conversion, which are presented in [15,24,25,28].

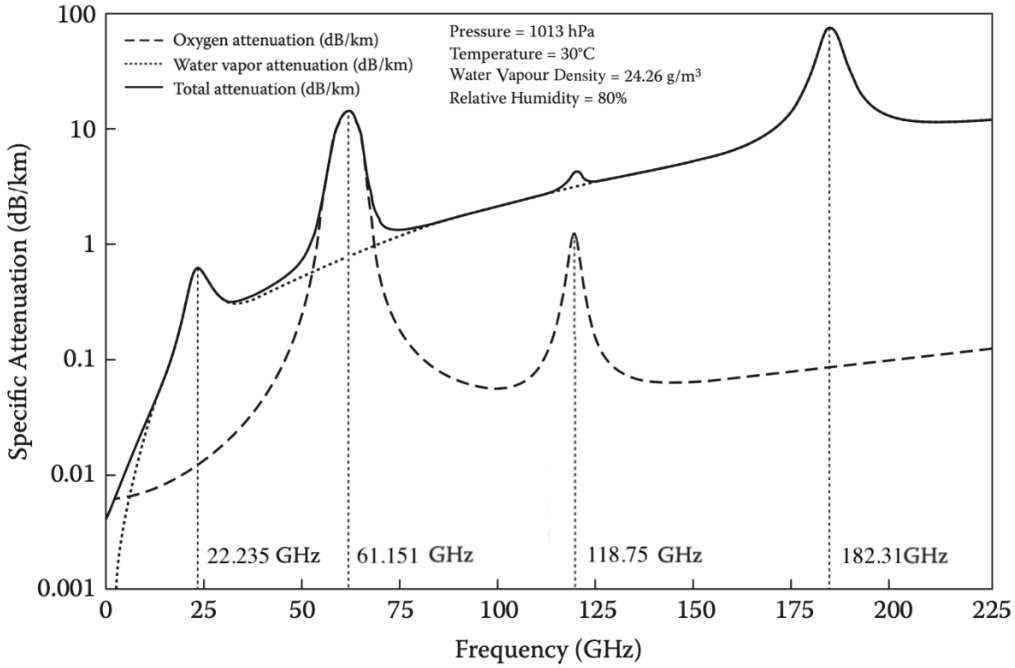

Figure 2 – Attenuation profile of the atmosphere due to water vapour and oxygen. Solid line represents attenuation caused by water vapour while dashed line represents attenuation caused by oxygen. Figure modified from [16].

Figure 2 is an example of an attenuation profile at sea level pressure (~1013 hPa). It is important to highlight that the atmosphere attenuation (or atmospheric absorption) is dependent on three parameters: the temperature, pressure, and water vapour density. From these, water vapour absorption is highly

dependent on the water vapour density (Figure 3) while oxygen absorption is dependent on the temperature and pressure [16,31]. For example, at the frequency of 118.75 GHz in extremely dry conditions, such as those found in polar regions, arid regions, high latitudes, deserts, and layers beyond the surface, the attenuation caused by water vapour will be somewhat lower than the attenuation caused by O_2 [16].

For this dissertation, the focus is the detection of the TCWV content for the final purpose of deducting WTC_{GB}. However, works using MWR_{GB} that aimed to detect TCWV were carried out years later [26,27,29,30]. These reports essentially used a dual-channel MWR_{GB} working in the water vapour absorption line at 21.0/22.235 GHz and in the cloud liquid absorption line at 31.40/31.65 GHz. This means that, the former band was used to detect the water vapour content and the latter to detect the liquid water content in the atmosphere (see Figure 3).

Different from the O_2, the water vapour absorption is due to the electric dipole transitions between rotational states of the water molecule. This behaviour leads to attenuation peaks in the microwave spectrum at 22.235 and 182.31 GHz (Figure 2; Figure 3) [16,24,28,31]. The sensing of liquid water, here, has the sole purpose of separating this component from the water vapour. Therefore, the use of the 31 GHz band is due to the fact that, the sky brightness temperature is two times more sensitive to liquid water than water vapour in this band (Figure 3). The need for this separation is mainly in cloudy conditions, as the atmosphere presents liquid water molecules integrated in clouds [16]. In other words, not using this frequency could bring an inconspicuous contribution of liquid water in the total absorption of the 22 GHz band [27].

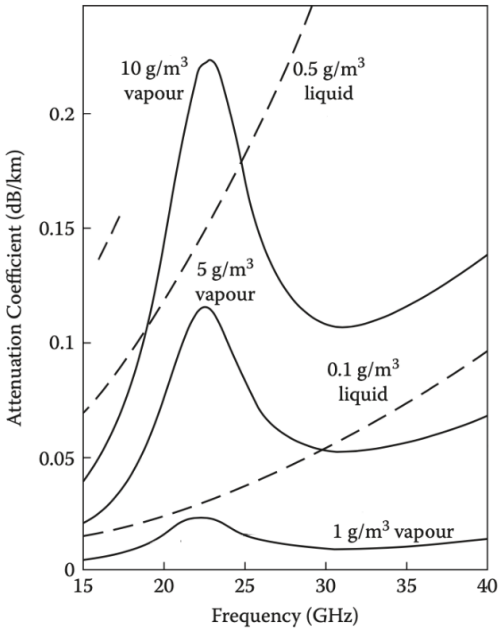

Figure 3 – Example of Attenuation profiles of the atmosphere for different densities of water vapour and liquid water. Solid lines represents attenuation caused by water vapour while dashed lines represents attenuation caused by liquid water. Figure retrieved from [24].

MWR_{GB} for TCWV and LWP observations, hence, have traditionally been developed for decades with the mentioned frequency ranges. However, the interest in more accurately detecting lower amounts of precipitable water vapour (TCWV < 5 mm) and cloud liquid (LWP < 50 $g.m^{-2}$) [32] has raised the need to explore some frequencies with higher sensitivity to these constituents. Recent studies suggest using

channels centred at 183.31 ±1, ±3, ±7, and ±14 GHz for retrieving small amounts of TCWV, in which the frequency of 183.31 ±14 GHz is especially for observing the cloud liquid contribution. This frequency range is 10-100 times more sensitive than the 22 GHz region. Nevertheless, due to the high sensitivity of this band, the channel response is saturated when the TCWV is nearly 5 mm [32,33]. Furthermore, the retrieved TB from these channels exhibit linearity with values of TCWV and cloud liquid over a limited range, for which nonlinear retrieval algorithms must be used [32]. In this same approach, when the interest in detecting low amounts of LWP exists, other works suggest the usage of higher frequency bands such as 90 and 150 GHz, which are 3-5 times more sensitive to cloud liquid than the 31 GHz region [33 - 35].

Considering the facts that, a large percentage of clouds have a LWP of less than 100 $g.m^{-2}$ [36] and the existence of weather conditions with TCWV often less than 3 mm such as in the cold Arctic winter [32], the use of these frequencies proves to be very necessary.

○ *Types of Ground-Based Microwave Radiometers (MWRGB)*

The specificities of the MWRGB will vary depending on the type of parameter that is intended to be observed, as well as the location where the equipment will be deployed due to the associated atmosphere conditions. Currently, there are different types of MWRGB for the different mentioned observations, among which low frequency channels are standard in commercial availability, such as the 22 and 31 GHz (dual-channel MWRGB) [33,34]. Table 1 lists the radiometers used in the Atmospheric Radiation Measurement (ARM) user facility - a network of climate instruments - and includes, for each device, the channel frequencies and the main retrieval parameters of interest. The presented radiometers are: Microwave Radiometer (MWR), Microwave Radiometer Profile (MWP), G-Band Vapor Radiometer (GVR), G-band Vapor Radiometer Profiler (GVRP), Microwave Radiometer-High Frequency (MWRHF), and Microwave Radiometer 3-Channel (MWR3C).

Table 1 - Types of MWRGB developed by the ARM with channel descriptions and retrieval parameters. Table adapted from [33]

	MWR	**MWRP**	**GVR**	**GVRP**	**MWRHF**	**MWR3C**
Channel Frequencies (GHz)	23.8, 31.4	22–60	183.3 ± 1,3,7,14	170–183.3	90, 150	23.8, 30, 90
Number of channels	2	12	4	15	2	3
Retrievals	TCWV, LWP	TCWV, LWP, Temperature Profiles	TCWV	TCWV	TCWV, LWP	TCWV, LWP
Date Range of deployment	1993 - present	2004 - present	2006 - present	2008 - present	2008 - present	2011 - present

- *The Atmospheric Radiation Measurement (ARM) user facility*

The ARM is a U.S. Department of Energy (DOE) Office of Science user facility. The program has been granting free data to benefit climate researchers for more than 20 years. The data represent the climatic conditions from different places around the world and are retrieved by instruments such as radars, lidars, and radiometers. Nowadays, the ARM observatories are located in three fixed sites: the Southern Great Plains (SGP), North Slope of Alaska (NSA), and Eastern North Atlantic (ENA) (at Azores, Portugal). Additionally, there are three mobile observatories with locations that are renewed after approximately 1 year anywhere in the world, except for one, the Oliktok Point (OLI) in Alaska (Figure 4), which is currently in extinction phase and is next to the NSA site, having a lifetime of more than 7 years. Lastly, there are aerial observatories that obtain aerial measurements above the fixed and mobile observatories [37,38]. Therefore, regarding MWRGB at these sites, over the years, ARM has implemented closely monitored calibration procedures and robust algorithms for TCWV retrievals in the zenith direction [33,36].

Among the MWRGB types implemented by ARM, MWR3C is the newest generation of 3-channel MWRGB and the only one that, for a long time, has been constantly measuring the atmosphere at two ARM fixed observatories, the SGP (2011 - present) and the ENA (2014 - present), as well as at one mobile observatory, the OLI (2013 - 2021) [33,38]. For this equipment, the TCWV retrieval from TB is performed from two methods: (1) Neural Network algorithm (NN), which uses non-linear statistical approaches to provide real-time retrievals and is trained with RS measurement datasets - using TB that are modulated from radiative transfer equations; and (2) the Microwave Radiometer Retrieval (MWRRETV2), an algorithm that provides retrievals through linear statistics, using as support, data from other collocated sensors (e.g., RS profiles), in order to obtain more accurate TCWV values. In addition, this latter algorithm computes and applies TB offsets to eliminate systematic biases [33].

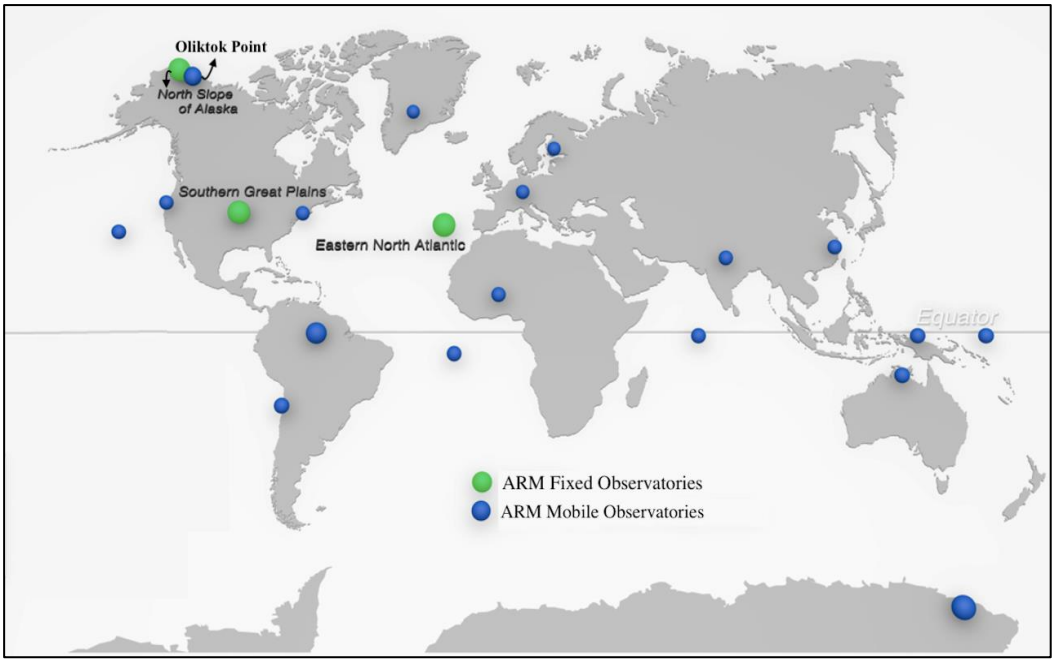

Figure 4 - Geographical representations of the ARM Observatories. Green represents fixed observatories while blue represents mobile observatories that are currently in operation or otherwise. Figure modified from [38].

Details of the NN architecture, results, and error analysis are available in [39] while the framework description of the first version of MWRRETV2 (MWRRET) is available in [36]. Due mainly to the latest generation of the 3-channel MWR_{GB}, some updates for the development of MWRRETV2 (version 2) were introduced, which are presented in [40]. In [33], an uncertainty evaluation was performed in order to compare both methods. The authors concluded that, the retrieval uncertainty produced by the MWRRETV2 method are halved when compared to the errors produced by NN. MWRRETV2 better performance is due to the additional information used to calculate the retrievals, and therefore, this method requires more computational capacity to run.

- *Estimation of the WTC from Ground-based radiometers (WTC_{GB})*

For this study, the TCWVs and TB retrieved from measurements of a 3-channel MWR_{GB}, have been collected from the ARM database. Post-process TCWV data with both algorithms (NN and MWRRETV2) have been considered. Additionally, the datasets collected are respective to the three observatories where the MWR3C equipment is installed for a significant period, which are ENA, SGP, and OLI [41,42] (Figure 4). All data are available in NetCDF or CSV format and each file corresponds to one day of measurements. The conversion from TCWV to WTC_{GB} have been carried out using the polynomial model described in [12], and adapted in [43] for retrieving the WTC in meters by entering TCWV value in cm:

$$\mathrm{WTC} = -(a_0 + a_1\mathrm{TCWV} + a_2\mathrm{TCWV}^2 + a_3\mathrm{TCWV}^3)\mathrm{TCWV}.10^{-2} \quad (3)$$

In Equation (3): $a_0 = 6.8544$; $a_1 = -0.4377$; $a_2 = 0.0714$; $a_1 = -0.0038$.

2.2 *Global Navigation Satellite Systems*

The troposphere has the characteristic of being a non-dispersive medium for radiofrequencies up to 20 GHz [44]. Therefore, the same ZTD that affects the main band of altimeter radar measurements (Ku band), at 13.5-13.8 GHz, also affects the signal emitted by other space geodetic techniques that operate at the same frequency region, such as GNSS, which uses frequencies between 1-2 GHz (L band) [13]. Since GNSS measurements depend on rigorously accurate solutions, ZTD products are calculate routinely at station location by dedicated Analysis Centers, such as those from the International GNSS Service (IGS) [45].

- *Determination of GNSS-derived ZTD*

In the GNSS internal processing, the ZTD is determined by means of Equation (4) [13]:

$$\mathrm{STD}(\varepsilon) = \mathrm{ZHD}\, m_{f_h}(\varepsilon) + \mathrm{ZWD}\, m_{f_w}(\varepsilon) \quad (4)$$

In Equation (4): STD = Slant Total Delay (m); *mfh and mfw* = hydrostatic and wet mapping functions, respectively; ε = elevation angle of the satellite relative to the GNSS station.

The ZTD is computed by the average delay of signals from a set of GNSS satellites [46], for a given instant (Figure 5). In general terms, the delay is measured by the time difference along the signal propagation between the satellite and the station receiver. Accordingly, in order to accurately resolve the time delay, the precise orbit and clock products of each satellite are used [47]. Furthermore, as Figure 5 shows, the signal path between each satellite and GNSS station is not in the zenith direction. Rather, a slant due to the azimuthal position of the satellite and its elevation angle (ε) occurs, resulting in the measured STD.

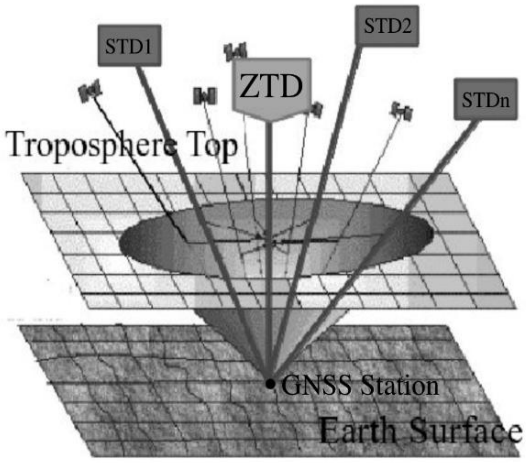

Figure 5 - Representation of the ZTD determination, for a GNSS station, from several STD products for a given time. Figure modified from [46].

In Equation (4), *a priori* ZHD at station location is estimated from available surface pressure measurement [7]. The pressure value is then Inserted in the modified Saastamoinen model [48], presented further in Equation (5). In the absence of in situ pressure observations, or in the context of ZTD processing centres, approximate values of pressure can be obtained from NWM [49]; *mfh* and *mfw* are known mapping functions (e.g., Global Mapping Functions and Vienna Mapping Functions 1) that have the role of re-project ZHD and ZWD to the slant direction. ZWD is the only unknown parameter in Equation (3), and therefore estimable. Each ZTD value is obtained as the sum of the *a priori* ZHD and the estimated ZWD. Uncertainties in determining the a priori ZHD can be absorbed by ZWD, thus, only the ZTD at the station location are highly accurate [7,13]. The ZTD are available with different temporal resolutions depending on the network. For example, in the IGS network, the delays are computed for a station at a cadence of 5 minutes.

○ *International GNSS Service (IGS)*

IGS is a voluntary organization that is part of the Global Geodetic Observing System (GGOS) of the International Association of Geodesy (IAG). Currently, IGS concentrates the information from 350 organizations spread over 118 countries, with a total of 506 GNSS stations in operation (Figure 6).

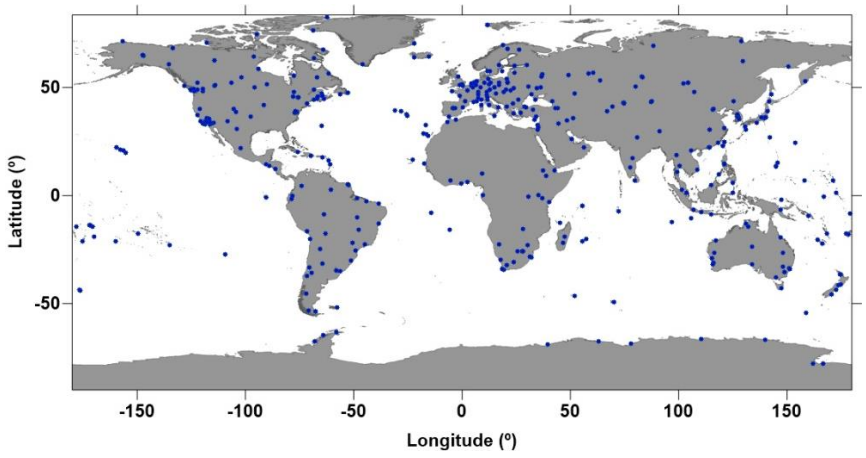

Figure 6 - Geographical locations of GNSS stations belonging to the IGS network in August 2021 [50].

This organization has been granting free data since 1994, aiming to benefit scientific, commercial, and educational institutions. The available data include: GNSS satellite ephemerides, satellite clock and tracking station information, earth rotation parameters, global tracking station coordinates and velocities, global ionosphere maps, and ZTD [50].

- *Estimation of the WTC from Global Navigation Satellite Systems*

The ZTD is a jointly contribution of the ZHD and ZWD components, and the ZHD is accurately estimated by other means [13]. Hence, the knowing of the ZWD (henceforth called WTC_{GNSS}) becomes possible. For this study, The WTC_{GNSS} extraction from GNSS-derived ZTD is described in four main steps, based on the study carried out by Fernandes et al., in [13]:

(1) Collecting GNSS-derived ZTD measurements for each station;
(2) Interpolating the ZHD values from NWM to the position and epoch of each ZTD measurement in (1), performing the appropriate reduction to the station height.
(3) Separating the ZHD component from the WTC_{GNSS}, both at station height;
(4) Whether necessary, reduction of the WTC_{GNSS} to the intended height.

As demonstrated in steps (2) and (4), height reduction must be performed separately for each component due to their distinct height dependencies. For example, the ZHD is easily modelled because its dependence with altitude is directly related to atmospheric pressure and temperature. In contrast, WTC has a large variability, as previously addressed in this work, and therefore is difficult to model [13]. However, Kouba, in [51], developed an empirical expression to model the dependence of WTC with height. Thus, whatever the purpose of using the WTC, such as an assessment between different techniques, a final reduction to the same height should be considered [51]. This procedure applies to all WTC sources, not just WTC_{GNSS}.

Additionally, the primary detail to be considered in step (2) is the determination of an accurate ZHD which can be obtained only by in situ surface pressure measurements or using interpolated values from MWM grids of sea level pressure, as evaluated in [13]. The same authors strongly recommended the use of ECMWF products for this purpose, due to their capacity in estimating the ZHD with a global-scale accuracy of 1-3 mm.

In this study, ZTD have been collected from GNSS stations processed by the IGS network. Subsequently, the extraction of the WTC_{GNSS} component has been performed following the foregoing steps, described, in detail below:

Step (1) is accomplished by collecting ZTD from tropospheric files, provided by IGS, of a given station.

In **step (2),** since ZHD is not a previously estimated field in the ECMWF gridded products, this delay is calculated using the mean sea level pressure (SLP) field - P_0, at sea level (h_0 = 0 m). Firstly, P_0 is interpolated - from ECMWF, in space and time for each instant and location of the ZTD collected in step (1). Then, the ZHD is calculated, in meters, for each instant, through the modified Saastamoinen model [48], Equation (5). However, Equation (6), presented in [52], must be applied previously in order to reduce the pressure at sea level to the pressure corresponding to the station altitude (P_S), in hPa.

$$\mathrm{ZHD} = \frac{0.0022768 P_S}{1 - 0.00266\cos 2\phi - 0.28 \cdot 10^{-6} h_S} \tag{5}$$

$$P_s = P_0 \left[-\frac{g_m (h_S - h_0)}{R_d T_m} \right] \tag{6}$$

In Equation (5) and (6): ϕ = geodetic latitude; h_S = GNSS station height (m); h_0 = sea level (m); R_d = specific constant for dry air (287.04 $J.K^{-1}.Kg^{-1}$) ; Tm = mean temperature (K); g_m= mean gravity ($m.sec^{-2}$).

Whenever height reduction is performed, the heights used must be in the same altitude system, ellipsoidal or orthometric. The parameter T_m is estimated by averaging the temperatures at altitudes h_0 and h_S. The temperature at h_0, which is at sea level, is given by the Global Pressure and Temperature (GPT) model [53]. The temperature at h_S is obtained by considering the value of -0.0065 $K.m^{-1}$ as the change rate of temperature with height. [53]. As in ECMWF products, the GPT utilisation requires interpolation in space and time.

Finally, g_m is calculated, in $m.s^{-2}$, with Equation (7) below [54]:

$$g_m = 9.784\,(1 - 0.00266\,cos\,2\varphi - 0.28 \cdot 10^{-6}\,h_s) \tag{7}$$

Step (3) is easily resolved by means of Equation (8) below:

$$\mathrm{WTC_{GNSS}} = -\,(\mathrm{ZTD} - \mathrm{ZHD}) \tag{8}$$

At last, **Step (4)** is performed to reduce the WTC correction, which is at the GNSS station height, to the required height, which in this study is the MWR_{GB} height. Accordingly, Equation (9) below is utilised, and it is important to highlight that the following equation has limitations for altitudes above 1000 meters and, therefore, should not be used in these situations [51].

$$\mathrm{WTC}(h_1) = \mathrm{WTC}(h_s) e^{\frac{h_s - h_1}{2000}} \tag{9}$$

In Equation (9): h_1 = MWR_{GB} height (m).

2.3 *On-board Microwave Radiometers*

Unlike the well-known ground-based radiometers algorithms, which retrieve amounts of TCWV as final products, the on-board radiometers algorithms, used in Satellite Altimetry, retrieve WTC_{OB} directly from the observed Brightness Temperatures (TB). In addition to this difference, some MWR_{OB} work with a third channel tuned at 18.7 GHz to complement the information obtained by the two traditional channels, tuned at a water vapour absorption line and at a cloud liquid absorption line. The inclusion of a low frequency channel is for inferring the wind-induced surface roughness effect. In the absence of this channel, such as in the MWR_{OB} of Sentinel-3 A/B and SARAL/AltiKa, this effect is usually determined using the altimeter-derived wind speed or the backscatter coefficient [2]. Additionally, the 18.7 GHz is currently used in the Jason-3 and Sentinel-6 reference missions, in the improvement of the WTC_{OB}

retrieval, due to the development of an algorithm by Brown [55]. This algorithm is capable of providing accurate corrections even with measurements of TB values contaminated with a land fraction up to 0.5.

- *Altimetry Missions With on-board Microwave Radiometer (MWROB)*

Table 2 presents the MWROB missions currently in operation and the channel frequencies these sensors are working with.

Table 2 - Description of the on-board microwave radiometer channels that are utilised by current altimetry missions. Table includes the launch year of each mission.

	SARAL/AltiKa	**Sentinel-3 A/B**	**Jason-3**	**Sentinel-6**
Channel Frequencies (GHz)	23.8, 37.0	23.8, 36.5	18.7, 23.8, 34.0	18.7, 23.8, 34.0/ 90, 130, 168
Number of channels	2	2	3	6 *
Date Range	2013 - present	2016/2018 - present	2016 - present	2021-present

***** Two on-board microwave radiometers on the satellite.

Sentinel-6, which is the fifth and newest generation of the reference missions, is in a non-sun-synchronous orbit with an inclination of 66.034° and at a referential altitude of 1336 km. This orbit coincides with all other reference missions (T/P and Jason-1/2/3) in order to ensure consistency of the collected data. This satellite performs nearly 13 orbits per day and has a same-site visitation latency of nearly 10 days, and therefore, has a large ground track separation of 315 km at equator. Sentinel-6 is the first Altimetry Satellite to have two MWROB: the Advanced Microwave Radiometer-Climate Quality (AMR-C), a 3-channel instrument (18.7, 23.8, and 34.0 GHz); and the experimental High Resolution Microwave Radiometer (HRMR), also a 3-channel instrument but of high frequencies (90, 130, and 168 GHz) which is intended to improve resolution in coastal regions [56].

Jason-3 was primarily designed to have a life expectancy of 5 years, however, expectations have already been exceeded. Since this satellite is the fourth generation of the reference missions, its orbit conditions are exactly as the foregoing descriptions. The Jason-3 MWROB is the Advanced Microwave Radiometer (AMR), a 3-channel instrument [57], similar to AMR-C.

The Sentinel-3 mission is a constellation of two satellites (A and B) with the difference in launch dates of nearly two years. Both satellites have an identical near-polar Sun-synchronous orbit and are separated by 140°, which improves the interleaving between both satellites for better mesoscale sampling. They are at a reference height of 815 km, inclination of 98.6°, and have a ground track separation of 104 km at equator. The time each satellite takes to revisit the same location is 27 days which is approximately halved when the measurements of both are considered. The MWROB of both satellites is the MWR (Microwave Radiometer), a nadir looking sounder with two channels [58]. One point to highlight is that after launch of Sentinel-3 B, the A/B pair entered into a tandem phase operation, in which both satellites were placed on near identical ground-track with a separation of 30 minutes in time. This phase lasted about 4-5 months in order to perform calibration and validation of the Sentinel-3 B observations.

SARAL/AltiKa MWR_{OB} is part of the AltiKa instrument, a dual-channel sensor. The mission was designed to have a Sun-synchronous orbit with an inclination of 98.538º and at a height of approximately 800 km. Also, a same-site visitation latency of nearly 35 days, 501 orbits within a cycle, and a ground track separation of 80 km at equator. However, due to mechanical problems, the planned orbit lasted until July 2016. The spacecraft could no longer maintain a repeated constant orbit and is currently in "orbit-drift" state [59].

- *Estimation of WTC from On-Board Microwave Radiometer*

For this study, WTC from On-Board Microwave Radiometer (WTC_{OB}) have been retrieved for the foregoing Altimetry missions, except for the Sentinel-6 mission which is currently in validation phase. Only measurements without contamination were considered, and this separation was accomplished through contamination flag parameters. However, no distance to coast criteria have been used. Therefore, the selected MWR_{GB} observations may include those that have been contaminated by land/ice since incorrect tracking of land-contaminated observations can occur. In such case, discrepancies will be observed in the comparisons results for which WTC_{OB} recovered from observations made close to land (up to 35 km) are used [6].

For comparison with WTC_{GB}, one point to highlight is the need to perform height reduction for the WTC_{OB} measurements, which are at sea level, to the MWR_{GB} height. This is performed by using Equation (9), with $h_S = 0$.

2.4 *Numerical Weather Models*

Numerical Weather Models (NWM) are a tool used to forecast parameters that determine the weather and climate. NWM, such as ECMWF or NCEP (National Centers for Environmental Prediction), use the assimilation of data from observations made by meteorological instruments in order to determine the atmospheric state that best reflects reality. Due to the chaotic nature of atmosphere, its prediction becomes of crucial importance in order to understand its dynamics and trends over time [61]. At fine resolutions, this chaotic nature also makes forecasting some parameters with no consistent behaviour more difficult, such as the TCWV. However, the accuracy of the models is becoming progressively better [62].

- *European Centre for Medium-Range Weather Forecasts (ECMWF) – ERA5*

The ECMWF is currently the world leader in global medium-range weather forecasting, producing several NWM on a global scale. ECMWF routinely processes data from about 800 million observations, among which are observations made by satellite instruments, surface and aircraft reports, Radiosondes, MWR_{GB}, etc. The TCWV can be retrieved by ECMWF's operational model - which is the High Resolution Atmospheric Model (HRES) with 0.125˚ x 0.125˚ spatial resolution and 6 hours temporal resolution, or the High Resolution Atmospheric Reanalysis (ERA5) with 0.25˚ X 0.25˚ spatial resolution and 1 hour temporal resolution [61]. Despite the HRES slightly outperforms ERA5 in most regions of the world, in extreme weather conditions ERA5 performs better due to its higher temporal resolution [63].

The ERA5 model is the fifth generation of global reanalysis, from 1979 to present. This model replaces the ERA-Interim reanalysis, with several improvements such as providing uncertainty estimates, using

several recently reprocessed datasets, and improving the temporal resolution to 1 hour instead of 6 hours [61]. However, regarding the use of the WTC_{NWM} a recent study concluded that time intervals do not have a significant impact on the retrieval of WTC from ERA5, for which a temporal resolution of 3 h sufficiently guarantees the same accuracy as 1 h [64]. The estimation of WTC_{NWM} from ERA5 grids is proposed by some methodologies, which are presented in [7,15,43,64] and will be described further in this subsection. Figure 7 represents the annual amplitude of the WTC_{NWM} for the entire globe.

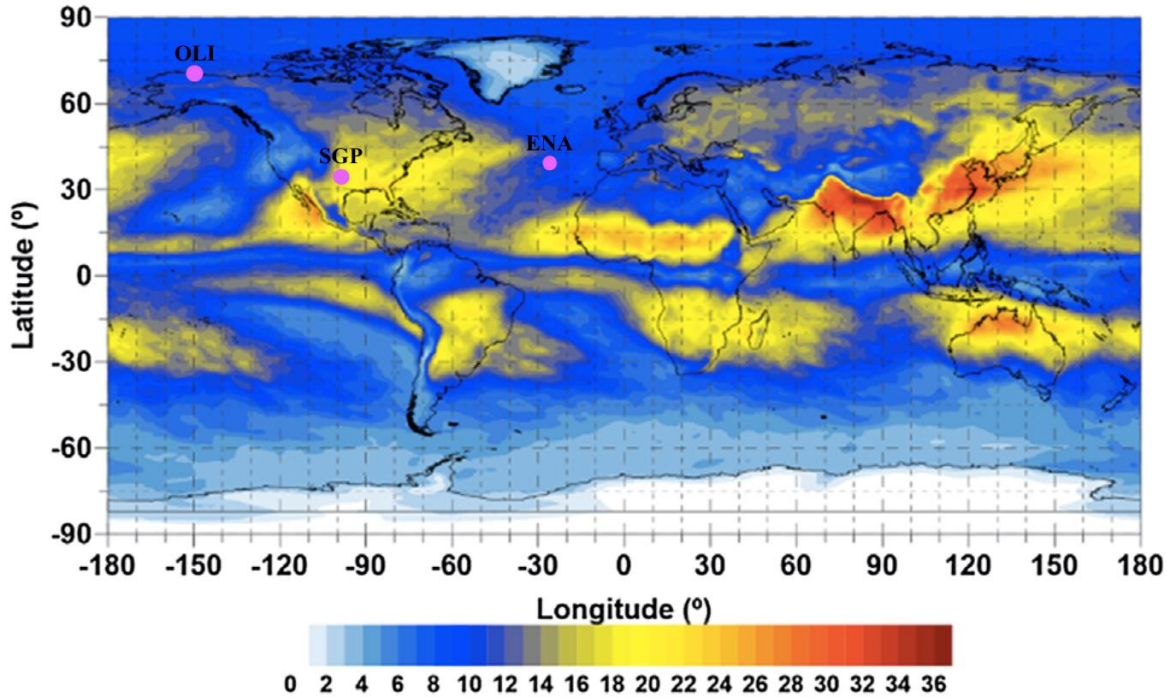

Figure 7 – Amplitude of the annual component of WTC_{NWM} (in cm), computed from the TCWV field of ERA5 *single-level parameters*. The location of the ARM observatories is represented in violet points. Figure modified from [15].

○ *Estimation of WTC_{NWM}*

The WTC_{NWM} can be directly calculated from *3D fields*, utilising the integral expression presented in [65], or by retrieving the TCWV from *single-level parameters* and then converted into WTC_{NWM}. The former method is the most accurate, which integrates the parameters such as pressure, specific humidity and temperature, of the various layers that constitute the ERA5 vertical column. The latter method is less computationally intensive, and therefore often preferred [7]. For this, the parameter TCWV is available at each node of the ERA5 single-layer grid and is expressed in $kg.m^{-2}$ or mm of water vapour. Then, the final conversion of TCWV values into WTC_{NWM} requires one of this two approaches: (1) an expression proposed by Bevis et al, in [66,67], which uses the TCWV and the mean troposphere temperature; or (2) using the polynomial model described by Stum at al., in [12] – Equation (3), which estimates the WTC directly from the TCWV values without any additional information [7,43]. Both approaches achieved similar results in an evaluation performed in [43], for which the values obtained by the "Bevis approach" are nearly 3% larger than for the "Stum approach". In addition, the authors raised the need to assess both approaches, with independent sources, in order to conclude which of the two methods achieves more accurate values.

In this study, the WTC_{NWM} values were retrieved from the ERA5 *single-level parameters*. Grids with spatial resolution of 025°x0.25° and temporal resolution of 3 h have been used to interpolate the TCWV values for each instant and location of the MWR_{GB} observations. Subsequently, the TCWV values have been converted to WTC_{NWM} with Equation (3), performing the appropriate height reduction with Equation (9). For this latter equation: h_S = MWR_{GB} height in the model's orography.

2.5 *Radiosondes*

As previously addressed in this study, radiosonde (RS) serve as a fundamental retrieval method for climate parameters such as temperature, pressure, geopotential height, relative humidity and wind parameters [7,21]. Since RS performs measurements in a vertical ascent from the ground, these are considered as in-situ measurements, reaching accuracies in the millimetre scale or even better [68]. Therefore, RS is the only instrument capable of performing in situ water vapour content measurements of the entire troposphere, enabling the retrieval of TCWV by integrating the various values collected at different heights. However, due to the great efforts necessary for the deployment of RS, their measurements have a low temporal and spatial resolution over the globe. For example, the RS launches are usually performed within 6 or 12 h depending on the schedule of the station, and therefore, the RS information is usually used for assessing other sources and also for calibrating other instruments that use radiometric technology [69].

Regarding the WTC_{RS} retrieved by RS, a point to highlight is that the fundamental measurement done by RS is the relative humidity (RH). Therefore, a proper conversion of RH to specific humidity is necessary in order to calculate the WTC_{RS} [7]. As in the NWM, the integral expression presented in [65] gives the possibility of directly computing the WTC_{RS} by utilising the parameters such as the pressure, specific humidity and temperature from the various altitude levels.

In some cases, the data retrieved from RS may include the so-called derived products, as it occurs in The Integrated Global Radiosonde Archive (IGRA) [70]. One of these products is the TCWV recovered from the integration of the water vapour content at the different altitudes measured by the equipment. For this case, the WTC_{RS} can be calculated either by the "Stum approach" or the "Bevis approach".

○ *The Integrated Global Radiosonde Archive (IGRA)*

The IGRA is a repository of radiosondes data and is managed by the National Oceanic and Atmospheric Administration (NOAA). The data are available for more than 2,800 stations, for which nearly 1000 are in operational state. Additionally, the observations are available for users in near real time from continuous measurements [70]. Figure 8 presents the Geographical locations of IGRA RS stations.

○ *Estimation of WTC_{RS}*

The radiosonde TCWV data have been collected from IGRA derived products. The complete time series of these data are made available in a single file, in ascii format, for each station. The TCWV values have been converted to WTC_{RS} with Equation (3), performing the appropriate height reduction with Equation (9). For this latter equation: h_S = radiosonde launching height.

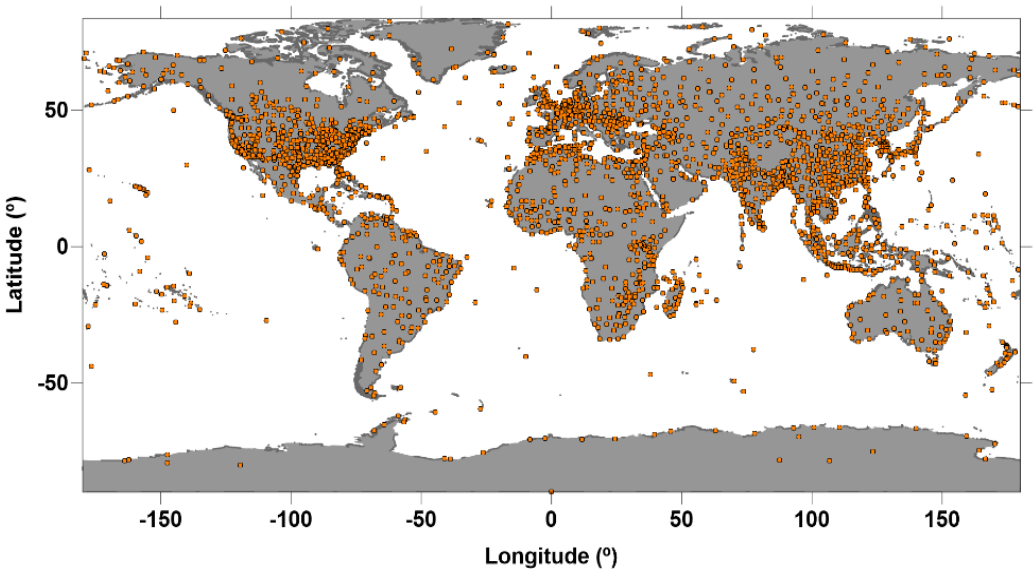

Figure 8 - Geographical locations of radiosondes launch sites belonging to the IGRA network in August 2021 [70].

3. Data description

The present section is organized in subsections that address the specificities of the data collected from each WTC source: ground-based MWR (3.1), GNSS (3.2), on-board MWR (3.3), ERA5 (3.4) and, Radiosonde (0).

Following the objectives proposed in this study, data have been collected from each source in order to conduct comparisons between the WTC obtained from the ground-based MWR (WTC_{GB}) observations, which are obtained from the different ARM observatories. As will further described, three observatories have been chosen to collect WTC_{GB} data, which were: ENA, OLI and SGP. Among these, only for the ENA site enough data from external sources to make all 4 comparisons were possible. On the other hand, for OLI and SGP sites, comparisons have been performed with only 2 external sources. For the former, NWM and on-board MWR, and for the latter, NWM and Radiosonde. In Figure 9, Figure 10 and, Figure 11 the spatial distribution of each source utilised per site are represented. It should be noted that all the satellites point measurements around the ENA and OLI observatories are shown Figure 9 and Figure 10 respectively. However, only measurements within the criteria defined in this work (described later) have been selected for the subsequent comparisons. Additionally, for these two observatories, samples from the SARAL/AltiKa mission were represented separately, due to their large spatial coverage, which is explained by the current SARAL "orbit-drift" state (subsection 2.3). Also, in subsection 2.3 the tandem phase of Sentinel-3 A/B pair is mentioned, in which both satellites were placed on near identical ground-track with a separation of 30 minutes in time. Therefore, in Figure 9 (bottom right) and Figure 10 (bottom) it is possible to observe Sentinel-3 B observations "overlapping" Sentinel-3 A observations, as well as Sentinel-3 B final ground-track offset by 140°.

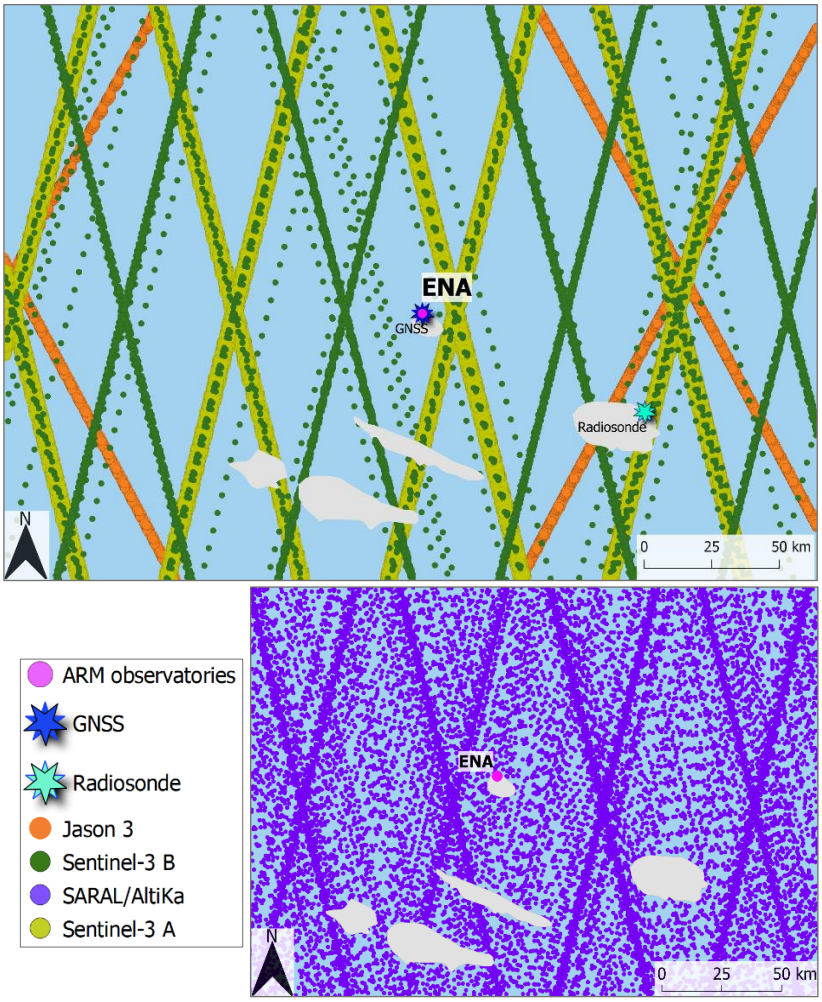

Figure 9 – Spatial distribution of the WTC sources around the ENA observatory – Azores, Portugal. Top figure: MWR_{GB} (ENA), GNSS, radiosonde, Jason-3, Sentinel-3 A and B. Bottom right figure: MWR_{GB} (ENA), SARAL/AltiKa. Bottom left figure: WTC source labels.

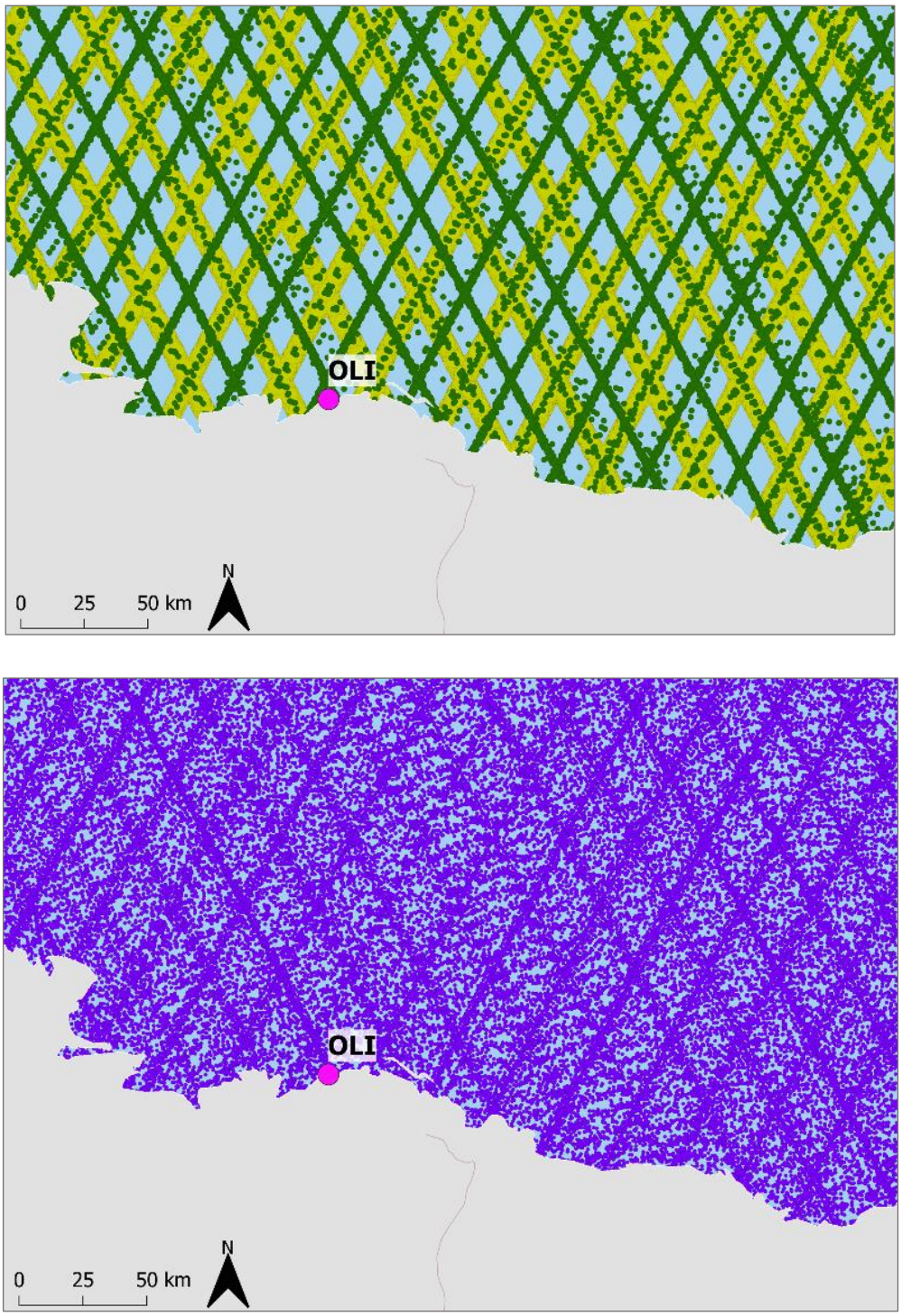

Figure 10 - Spatial distribution of the WTC sources around the OLI observatory – Alaska, U.S. Top figure: MWR$_{GB}$ (OLI) and Sentinel-3 A and B. Bottom figure: MWR$_{GB}$ (ENA), SARAL/AltiKa. For this figure, the WTC source labels are the same as for Figure 9.

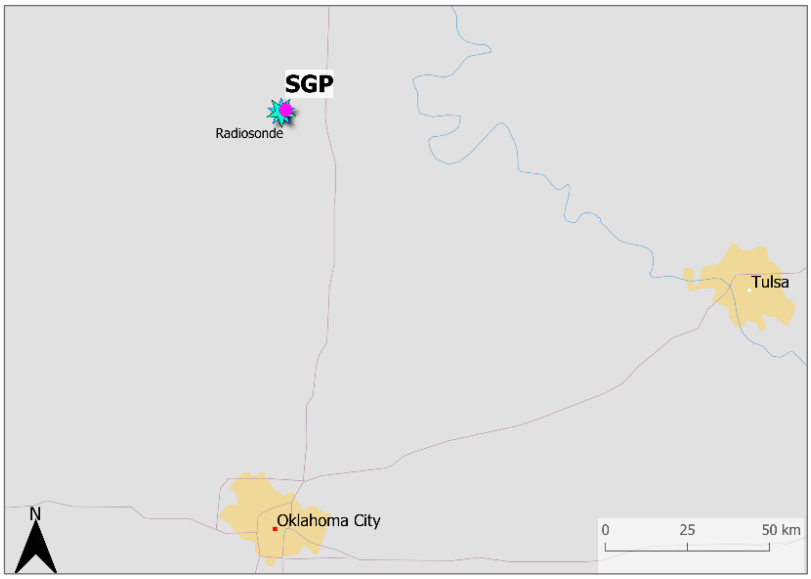

Figure 11 - Spatial distribution of the WTC sources around the SGP observatory – Oklahoma, U.S.: MWR$_{GB}$ (SGP) and radiosonde. For this figure, the WTC source labels are the same as for **Figure** 9.

3.1 *Ground-based radiometer data from ARM*

As explained above, ground-based radiometer (MWR$_{GB}$) data have been used from three observatories: ENA, OLI and SGP. The deduced WTC$_{GB}$ data for these three observatories have been computed and presented in Figure 12. These data represent the complete time series of MWR$_{GB}$, with temporal resolution of approximately 3 - 5 seconds for the ENA and OLI observatories while for SGP it is approximately 11 - 15 seconds. The data temporal availability are different, since the NN algorithm computes WTC$_{GB}$ in near real time (latency of 2 days) and the MWRRETV2 algorithm can have a Latency of more than 1 year.

Additionally, observations flagged as contaminated by rain or as invalid have been previously screened out. Accordingly, the final number of observations for each observatory was: ENA (NN) - 47,643,797; ENA (MWRRETV2) - 39,728,820; OLI (NN) - 46,702,309; OLI (MWRRETV2) - 35,683,579; SGP (NN) - 20,496,260; SGP (MWRRETV2) - 18,686,295.

Two points to highlight are that, the time series for the SGP observatory has a gap in observations at the end of 2020, and for 2021, despite having available observations, the ARM has advised against using them. This is due to the installation of a new MWR$_{GB}$ at the SGP observatory, and therefore calibration evaluations of the instruments are still being carried out. Table 3 presents the geographical positions of the MWR$_{GB}$ instruments installed in the respective observatories.

Table 3 - Geographic locations of the observatories ENA, OLI and SGP. Latitude and longitude are in decimal degrees and Height is above mean sea level.

Observatory	Latitude (º)	Longitude (º)	Height (m)
ENA	39.092	-28.026	30.48
OLI	70.495	-149.886	2.0
SGP	36.606	-97.485	316.0

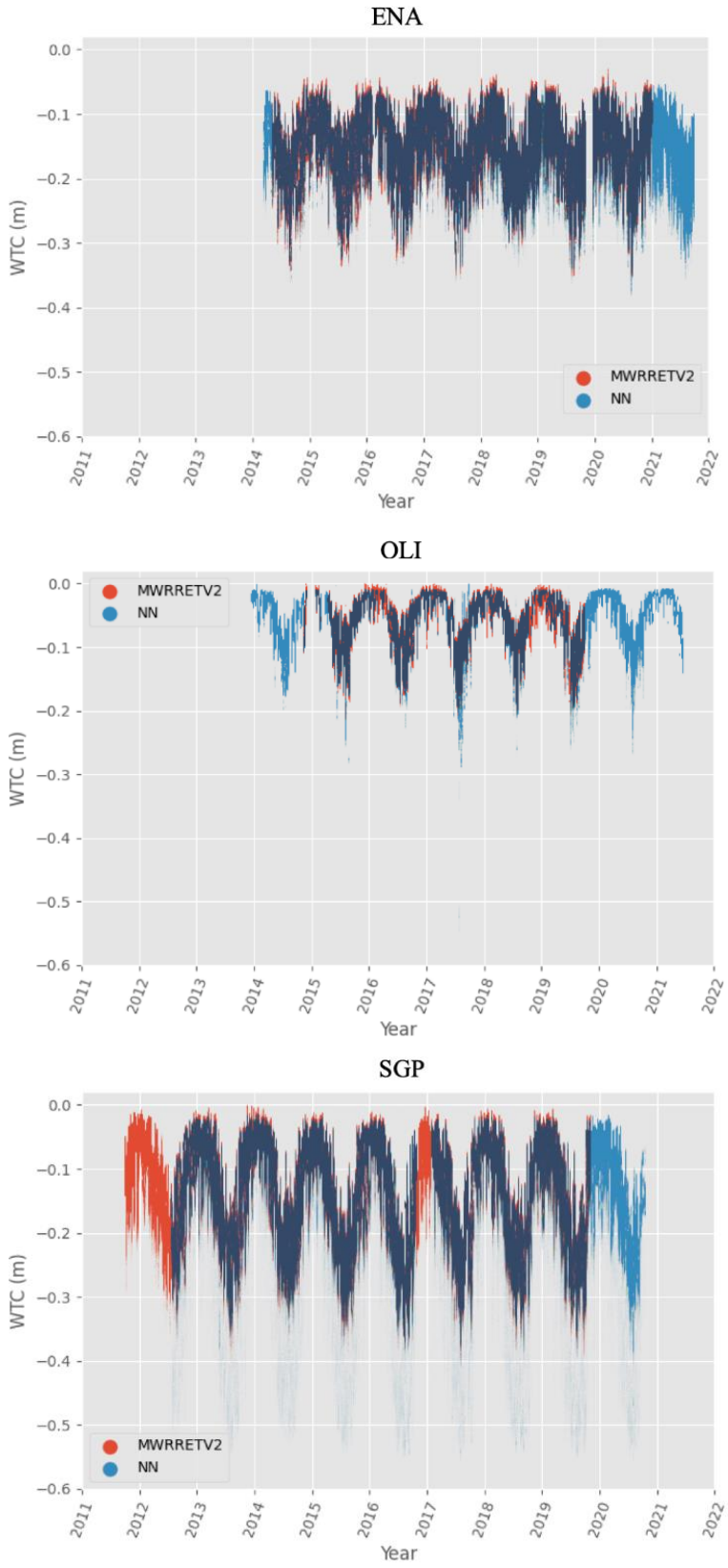

Figure 12 - Complete time series of the observatories ENA (top), OLI (centre) and SGP (bottom). The graphs are WTC_{GB} values deduced from the NN (in blue) and MWRRETV2 (in red) algorithms where points with a darker shade of blue are measurements overlapped between algorithms.

3.2 *Wet Tropospheric Correction from GNSS*

In order to obtain Wet Tropospheric Correction from GNSS measurements (WTC_{GNSS}) comparable with WTC_{GB}, two criteria were used to choose the IGS GNSS station. The first is the temporal compatibility of the data for at least one year, in order to obtain representative data of the annual WTC variability. The second criteria is the closest station up to 100 km, due to the spatial correlation scale of the WTC ranging from 40 to 93 km, depending on the location [71]. Indeed, both criteria also applies to other comparable WTC sources - MWR_{OB}, GNSS, and RS, with the exception of NWM which has the advantage of interpolating values at any time and place on the globe.

Among the three observatories, only for ENA it was possible to obtain a station that met the two criteria. Table 4 presents the GNSS station (ENAO) chosen for the ENA observatory, including other relevant details for this work.

Table 4 – Details of ENAO – IGS GNSS station. Table includes Latitude and longitude in decimal degrees and Height above geoid (orthometric height).

IGS station	Latitude (º)	Longitude (º)	Height (m)	Distance from ENA (m)	Date range
ENAO	39.091	-28.026	33.18	51.0	February 28, 2020 – June 06, 2021

3.3 *Wet Tropospheric Correction from on-board MWR*

For this study, the WTC_{OB} data have been retrieved from the Radar Altimeter Database System (RADS), which was developed at Delft University of Technology's Department of Aerospace Engineering and is currently maintained and updated jointly by the NOAA Laboratory for Satellite Altimetry and EUMETSAT [60]. RADS groups the data from all altimetric missions to the present days and is available in netCDF files format - one for each satellite pass. The datasets provide several parameters needed to construct the Sea Level Anomaly (SLA) for each coordinate and time observed by the satellite in its own track.

Different altimetry missions possessing on-board radiometers, available in RADS were chosen for the different sites under analysis. Except for the SGP site, since the entire region around this observatory is terrestrial, and thus there is a lack of valid WTC measurements from on-board microwave radiometers. The selection was based on the existence of considerable valid WTC_{OB} measurements up to 100 km from the MWR_{GB}. In Table 5, the set of altimetry missions selected for each observatory is presented.

Table 5 - List of altimetric missions used in the comparison with MWR$_{OB}$ for the OLI and ENA observatories.

ARM observatory	Satellite Altimetry Missions
ENA	Sentinel-3 A and B; SARAL/AltiKa; Jason-3
OLI	Sentinel-3 A and B; SARAL/AltiKa

3.4 *Wet Tropospheric Correction from ERA5*

As explained above, the Numerical Weather Model used in this study is ERA5, provided as global grids at 0.25° X 0.25° spatial resolution and 3 h temporal resolution. The Mean and Standard Deviation (StD) of WTC$_{NWM}$ values calculated from TCWV of ERA5 model allow characterizing the variability of this component over the different regions of the globe (Figure 13). For this study it is important to characterize the variability of WTC$_{NWM}$ in the observatories ENA, OLI and SGP. For this, Mean and StD values of WTC$_{NWM}$ along one year were interpolated to their respective locations and presented in Table 6.

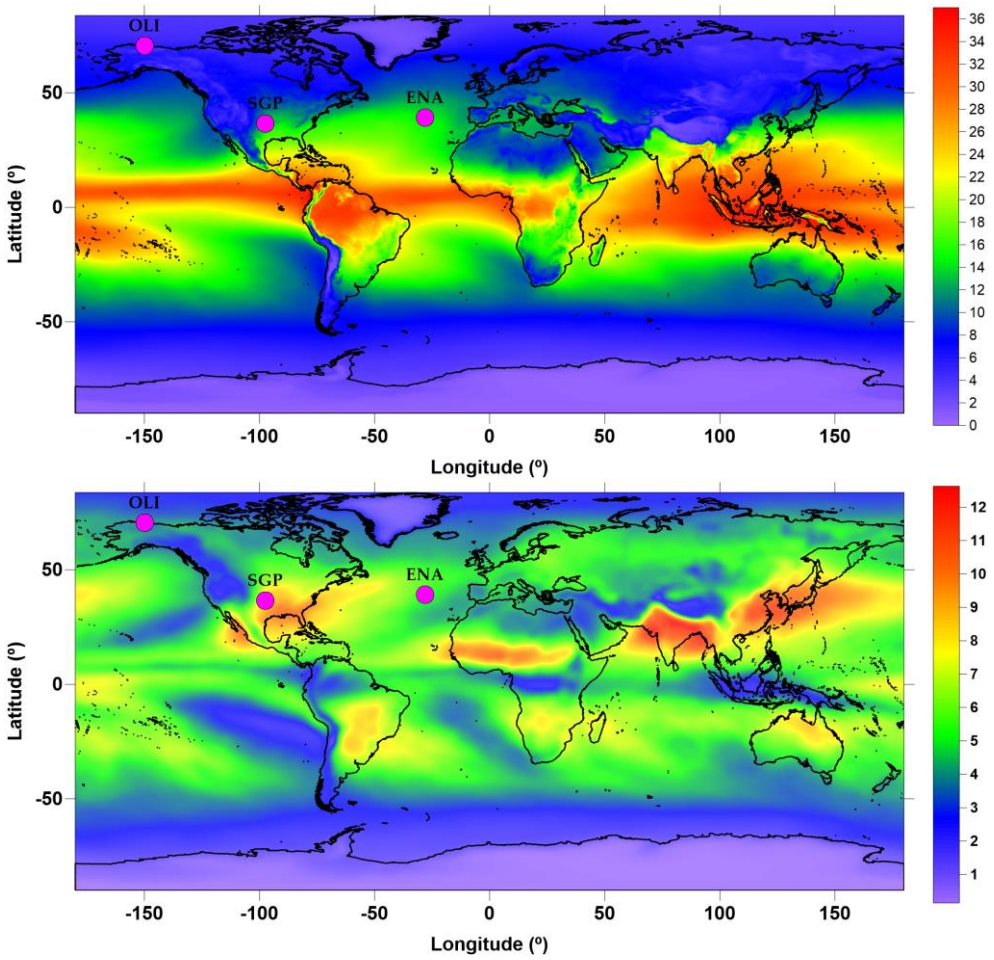

Figure 13 - Mean (top) and StD (bottom) of WTC$_{NWM}$ (in cm), computed from the TCWV field of ERA5 *single-level parameters* over a period of one year. The location of the ARM observatories is represented in violet points.

Table 6 - Interpolated Mean (absolute values) and StD values of WTC_{NWM} along one year for the ENA, OLI and, SGP observatories.

Observatory	Mean (cm)	StD (cm)
ENA	14.62	5.33
OLI	5.56	4.15
SGP	13.57	8.54

3.5 *Radiosonde data from IGRA*

Table 7 shows the list of radiosonde (RS) stations selected to compare with the WTC_{GB} data from the ENA and SGP observatories. IGRA stations were not found within 100 km of the OLI observatory, so this observatory was excluded from the comparison with RS. The temporal resolution of the LAJES station measurements is 12 hours while the LAMONT station conducts launches every 6 hours.

In the final stages of this study, a fully collocated station with OLI observatory measurements was found in ARM, however the products were not integrated into TCWV, so this methodology could not be added to this study in the available time.

Table 7 - List of RS stations used in the comparisons (WTC_{GB}, WTC_{RS}) for ENA and SGP observatories. Table includes Latitude and longitude in decimal degrees and Height above geoid (orthometric height).

IGRA Stations	Latitude (º)	Longitude (º)	Height (m)	ARM Observatory	Distance from ARM (km)	Date range
LAJES (AZORES)	38.78	-27.086	73.0	ENA	89.1	September 10, 1946 – September 04, 2021
LAMONT	36.60	-97.50	306.0	SGP	1.50	January 01, 2000 – October 04, 2021

4. Assessment of the WTC from Ground-Based Radiometers

This section presents the methodological approach used, as well as the results found in this study. In the first subsection (4.1), the methodologies used in the comparison between the Ground-based radiometers and external sources (ERA5 model, on-board MWR, Radiosondes and GNSS) will be addressed. The results from these comparisons have been organised by subsections, which are: comparison with the ERA5 model (4.2), comparison with on-board MWR (4.3), comparison with radiosonde data (4.4), and comparison with GNSS-derived wet tropospheric corrections (4.5). Each result will be accompanied by a description of what it is intended to present visually. In addition, a discussion of these results is provided at the end of each subsection.

4.1 Methodological Approach

The main data analysis was executed through scientific programming in Python language, with only a minor part in MATLAB. In order to provide cross-analysis between the WTC_{GB} values and the WTC obtained from other sources, care has been taken to collect temporally correlated datasets. Then, the observation acquisition times for each dataset have been transformed to MJD (Modified Julian Date) format, which counts the days (including its fractional part) elapsed after the Epoch defined as November 17, 1858, 00:00:00 (UTC).

In this dissertation, the comparisons of WTC_{GB} with external sources is carried out by creating four assessment pairs – (WTC_{GB}, WTC_{OB}), (WTC_{GB}, WTC_{GNSS}), (WTC_{GB}, WTC_{RS}), and (WTC_{GB}, WTC_{NWM}). For the only spatial and temporal fully collocated comparison posed by interpolation - (WTC_{GB}, WTC_{NWM}), linear (time) and bilinear (spatial) interpolation procedures have been performed to calculate the WTC_{NWM} values for each WTC_{GB} instant. For the comparisons that can be collocated or not, the closest WTC_{GB} value in time was selected for each external source value. The ground-based radiometer data have a temporal resolution of nearly 3 - 15 seconds, which depends on the equipment configuration in each observatory. Given this fine temporal resolution, the time series of MWR_{GB} observations have been resampled for every 3 minutes, totalling approximately 100,000 observations per year.

Concerning the water vapour high variability in space and time, and following previous works in the context of altimetric measurements validations [2,6,71], two thresholds have been considered to mitigate the non-collocation effect: (1) time differences of measurements up to 30 minutes; and (2) measurements up to 100 km from the MWR_{GB} location. Due to the high temporal resolution of MWR_{GB}, temporally collocated measurements with other sources will always exist, except in cases where there are data gaps in the MWR_{GB} time series. This may happen, for example, due to unavailability of input data into algorithms; or, graphically less expressive, due to observations made during rainy periods. Measurements contaminated by rain have been removed using the observations quality flags, or through known thresholds in the literature such as the rain rate < 2 mm/h and TB of the 30 – 31 GHz band < 100 K [72].

The WTC_{GB} have been computed from the TCWV values, which were retrieved from the NN and MWRRETV2 algorithms, using the "Stum approach", equation (3).The MWR_{GB} observatories chosen for collecting the TCWV datasets were ENA, SGP, and OLI (Figure 4), due to the significant period in which the MWR3C equipment has been deployed and collecting information at these locations. Thus, the comparisons have been carried out in parallel for each observatory and algorithm. The number of comparisons performed for each observatory varied depending on the availability of data from external sources that fell within the previous defined temporal and spatial thresholds.

Subsequently, WTC differences have been computed for each comparison, and statistical analyses (described below) were performed. Furthermore, the comparison with MWR_{OB} (WTC_{GB}, WTC_{OB}) have been analysed as a function of the distance between the measurements of the two sensors. This is due to the fact that MWR_{OB}, conversely to others sources, vary both in space and time. Thus, WTC_{OB} values have previously been clustered in 20 km distance intervals from the MWR_{GB}. The following intervals have been considered: [0 - 20 km], [20 - 40 km], [40 - 60 km], [60 - 80 km], [80 - 100 km]. This decision to cluster the measurements serves to achieve one of the objectives proposed in this work: evaluation of how the distance between the ground-based and on-board radiometers affects the stability of the former (WTC_{GB}) for Satellite Altimetry.

○ *Statistical Analysis*

For each comparison, differences were computed between the WTC_{GB} and each external source. From these differences, various statistical parameters are calculated: Mean (or bias), Standard Deviation (StD), Minimum, Maximum, and Root Mean Square Error (RMS).

In order to obtain an intra-algorithm comparison (NN and MWRRETV2), the samples were temporally paired between them. In other words, only observations temporally collocated between algorithms have been used for the statistical analyses. Except for the comparison with NWM (WTC_{GB}, WTC_{NWM}), in which the daily RMS was calculated. Due to the full ability to interpolate the WTC_{NWM} values for all WTC_{GB} instants, the daily RMS analysis allows to graphically observe the level of agreement between both sources over the entire time series. In addition, the comparison with NWM (WTC_{GB}, WTC_{NWM}) was also analysed for the entire time series of each algorithm.

Recalling that the time period for the GNSS data availability is approximately 15 months, statistical analyses with this integral time was only possible for the NN algorithm. This was due to the facts that, the GNSS station (ENAO) started producing ZTD data recently (February 28, 2020) and the MWRRETV2 algorithm does not have data available for the year 2021.

○ *Wet Tropospheric Corrections Directly Estimated from Ground-Based Radiometer Observations*

Additionally, only for the ENA observatory, TB data from ground-based MWR have been also collected in order to train a new neural network algorithm, which has been developed within this dissertation. The algorithm framework was taken from a study developed by Vieira et al., in [73], in which the authors tuned the algorithm to retrieve WTC_{OB} for the Sentinel-3 mission.

The neural network technique has been implemented in the past for the Envisat mission and is being used in the Sentinel-3 mission to retrieve the WTC from on-board radiometer observations [74]; as well as

for ground-based radiometers in which the neural network algorithms is used to estimate the preceding variable of WTC, the TCWV (subsection 2.1). The correct establishment of WTC values from TB, is due to the NN technique principle lying in being capable of estimating values from non-linear relationship between variables, as is the case of WTC and TB [75].

In the present study, WTC retrieved from ground-based MWR (WTC_{OB}) is based on at least two well-known steps, which are: (1st) deducing TCWV values from the Brightness Temperatures using the NN or MWRRETV2 algorithm; and (2nd) converting TCWV to WTC_{GB} with Equation (3). Accordingly, this new algorithm has been trained aiming to estimate the WTC directly from the TB observed by the MWR_{GB} channels.

In order to evaluate the best combination of inputs to be used in this novel algorithm, two versions were created: (1) using 2 inputs - TB from both 23.8 and 30 GHz channels (henceforth called WTC_{GB_2TB}); and (2), using 3 inputs - inclusion of the TB from the 90 GHz channel (henceforth called WTC_{GB_3TB}). Thus, the training dataset consisted of 100,000 samples which refer to 1 year of observations, 3 or 2 TB as inputs, and model-interpolated WTC (WTC_{NWM}) for the same instants as output.

WTC retrievals from WTC_{GB_2TB} and WTC_{GB_3TB} will be assessed independently with WTC_{GNSS} values. For that, statistical analyses have been applied on the WTC differences. Lastly, a comparative analysis of these results was performed along with the previous results obtained from the same comparison with GNSS (WTC_{GB}, WTC_{GNSS}) carried out with the NN algorithm for the ENA observatory (subsection 4.5).

4.2 *Comparison with Numerical Weather Model*

This section presents the comparison between the WTC from the ground-based radiometers and those from the ERA5 NWM. This comparison (WTC_{GB}, WTC_{NWM}) was carried out for all observatories (ENA, SGP and OLI). The results shown in Figure 14, Figure 15, and Figure 16 are respective to the daily RMS of the differences between the WTC_{GB} computed from the NN and MWRRETV2 algorithms against the WTC_{NWM}. Additionally, Table 8, Table 9, and Table 10 present the statistical parameters of these comparisons. For these, the global statistics of the entire time series are presented for each algorithm individually.

Figure 14 shows that the RMS values, for the measurements performed at the ENA observatory, have a seasonal behaviour. Maximum RMS values are founding during the middle of the year when summer occurs in the North Hemisphere. In contrast, minimum RMS values occur during the beginning and end of the year, respective to the coldest months. Although this seasonal behaviour can be observed, it is expressed with a weak seasonal signal, which differs from the results observed below, for the SGP and OLI observatories, for which the seasonal signal is more pronounced

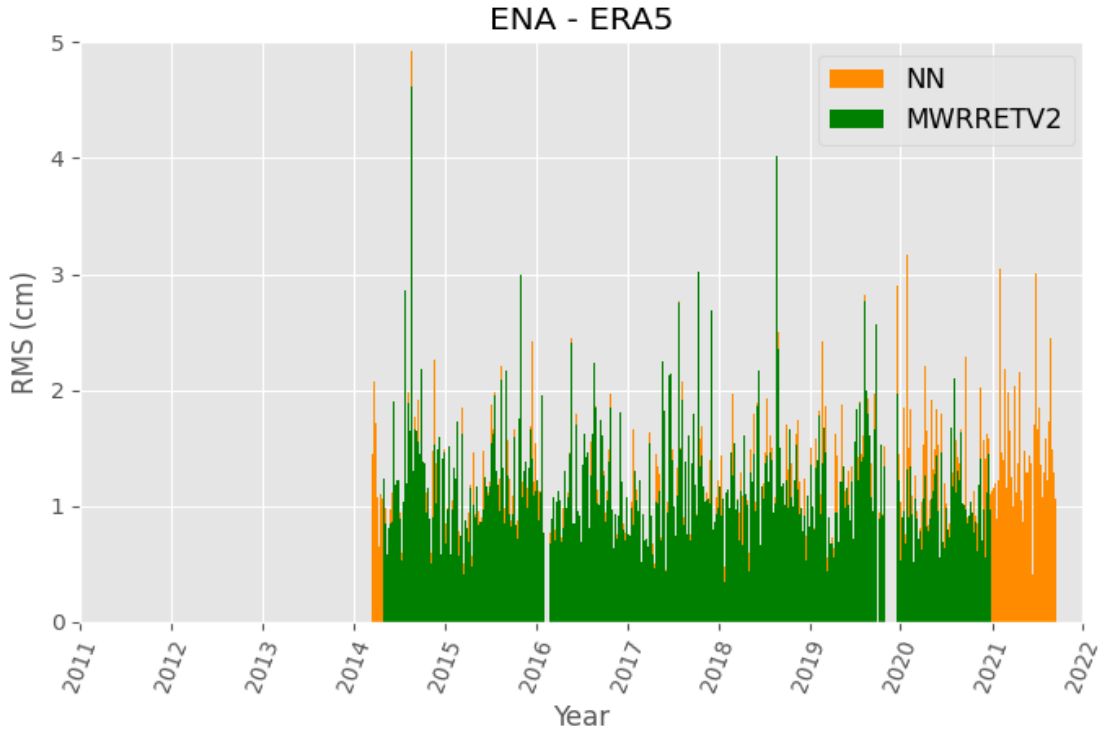

Figure 14 - RMS of the daily WTC differences between the products of the ARM algorithms and the ERA5 climate model, for the ENA observatory.

Table 8 shows that the global statistics of the differences for the MWRRETV2 algorithm obtained better agreement with ERA5. The Mean and StD values of the differences were lower than those obtained in the assessment of the NN algorithm. The same behaviour is observed for the maximum and minimum values of the differences, in which the NN algorithm presented, in absolute terms, higher values compared to MWRRETV2.

Table 8 – Global statistics of the WTC differences between the products of the ARM algorithms and the ERA5 climate model, for the ENA observatory.

	Samples	Mean (cm)	StD (cm)	RMS (cm)	Min (cm)	Max (cm)
NN	761,451	-0.48	1.09	1.19	-10.75	9.73
MWRRETV2	677,017	-0.35	1.04	1.09	-8.31	9.35

The RMS values for the OLI observatory are graphically represented in Figure 15. For this observatory, a strong seasonal signal is observed. Again, the RMS values reach higher magnitudes in the warmer months of the year while very lower RMS are found in the colder months. Also, for some days between the years 2017 and 2018 there was a significant number of RMS values above 2 cm, with one of the days reaching a value close to 5 cm. This situation is observed only for the NN algorithm, while for the same period, MWRRETV2 kept the RMS below 1 cm, or only slightly above this mark.

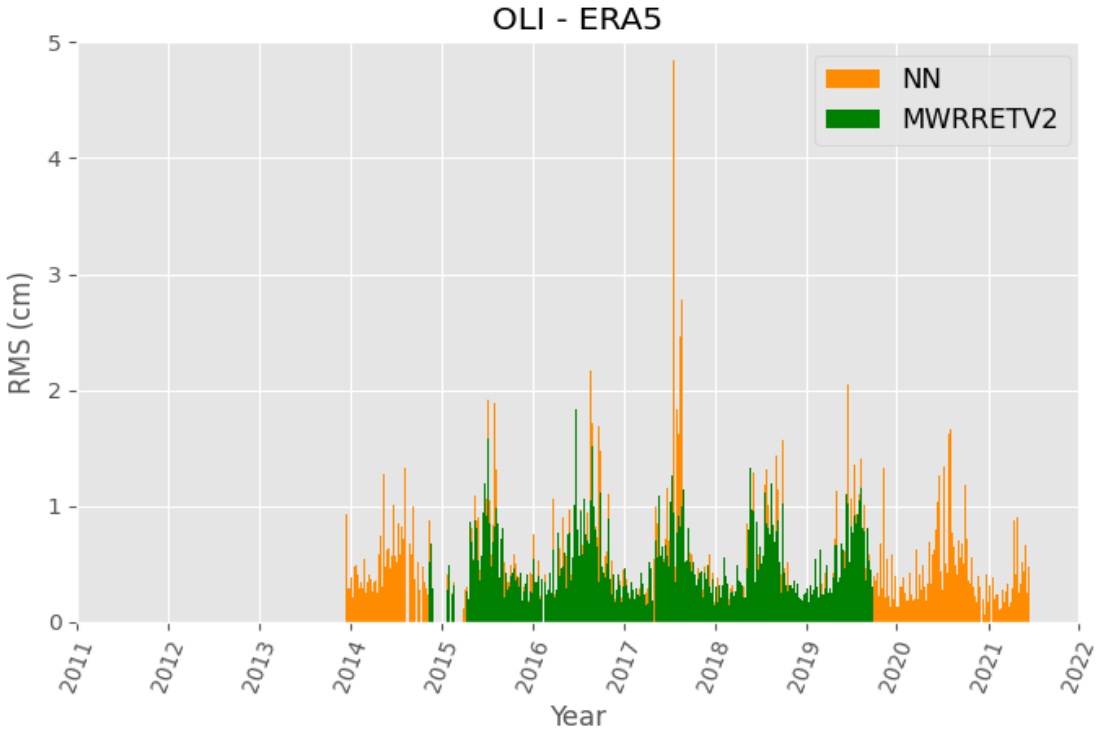

Figure 15 - RMS of the daily WTC differences between the products of the ARM algorithms and the ERA5 climate model, for the OLI observatory.

Table 9 demonstrates that just as for the ENA observatory, the global statistics for the OLI observatory showed a better agreement between the WTC_{NWM} and the WTC_{OB} retrieved from the MWRRETV2 algorithm than with the corresponding WTC_{OB} from NN. However, for this observatory the order of magnitude of the mean and StD statistics are quite low with Mean differences close to zero and StD around 0.5 cm. The maximum and minimum difference values of the results with the NN algorithm again prove to be higher, in absolute terms, when compared to those of MWRRETV2. Additionally, it is important to highlight that the number of samples in the MWRRETV2 algorithm assessment is almost 2/3 of the number of samples considered for the NN algorithm. This high difference of samples is due exclusively to the different data availability by the ARM.

Table 9 – Global statistics of the WTC differences between the products of the ARM algorithms and the ERA5 climate model, for the OLI observatory.

	Samples	Mean (cm)	StD (cm)	RMS (cm)	Min (cm)	Max (cm)
NN	740,021	-0.114	0.54	0.56	-37.97	9.33
MWRRETV2	476,992	0.0820	0.50	0.50	-4.94	4.10

The RMS values for the SGP observatory are graphically illustrated in Figure 16. Among all the three evaluated sites in this subsection, the results for this observatory had the largest amplitudes of the WTC differences. Furthermore, the seasonal variations of the RMS values were the most expressive,

demonstrating higher RMS values in the months characterized by high temperatures for the North Hemisphere. By overlaying the two considered differences, it was possible to observe that RMS values for the MWRRETV2 algorithm remained mostly lower when compared to the results obtained with the NN algorithm.

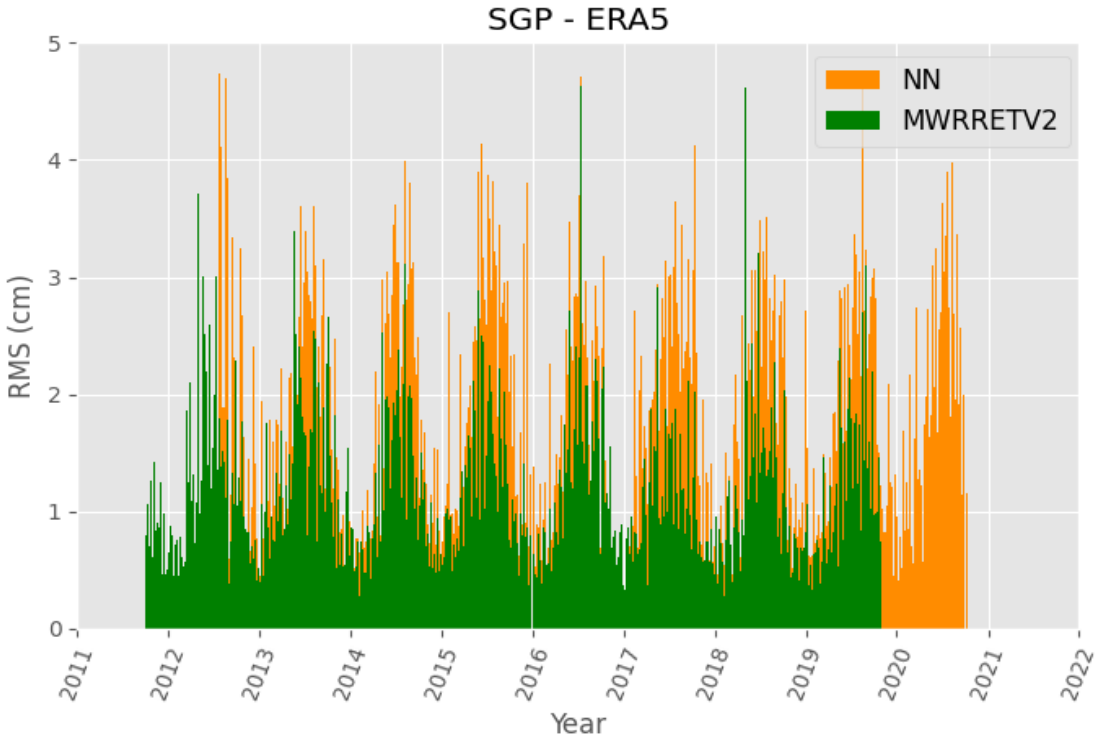

Figure 16 - RMS of the daily WTC differences between the products of the ARM algorithms and the ERA5 climate model, for the SGP observatory.

This better agreement of the MWRRETV2 algorithm with ERA5 is reinforced by the global statistics parameters, which are present in Table 10. The mean and StD difference statistics are largely lower for this algorithm when compared to NN. While the mean difference obtained by NN reached approximately 0.3 cm, in absolute value, the MWRRETV2 algorithm obtained a value very close to zero. Additionally, the StD statistics for MWRRETV2 was approximately 0.75 cm lower than that obtained by the NN (1.86 cm), which reached the highest StD value among all the observatories evaluated in this subsection

Table 10 – Global statistics of the WTC differences between the products of the ARM algorithms and the ERA5 climate model, for the SGP observatory.

	Samples	Mean (cm)	StD (cm)	RMS (cm)	Min (cm)	Max (cm)
NN	810,293	-0.30	1.86	1.89	-36.12	17.43
MWRRETV2	825,734	0.07	1.18	1.18	-13.15	12.72

- *Discussion*

The graphical results (Figure 14 - Figure 16) and the statistical parameters for the comparison (WTC_{GB}, WTC_{NWM}) (Table 8 - Table 10) showed a seasonality of the RMS values of the WTC differences for all observatories, with the maximums in the warmer months and minimums in the cooler months. This seasonality can be explained due to the greater temporal and spatial variability of water vapour during summer [76], occurring the opposite in winter.

In addition, for all results, the MWRRETV2 algorithm obtained a better agreement with the ERA5 model. Nevertheless, drawing conclusions of performance superiority of MWRRETV2 algorithm over NN cannot be sustained in this comparison (WTC_{GB}, WTC_{NWM}). Accordingly, since NWM reproduce a smoothed version of the chaotic atmosphere, the better agreement between MWRRETV2 and the ERA5 model could actually indicate that this algorithm is producing smoother retrievals than the NN.

As already discussed in this study, point measurements from sensors are expected to be more accurate than interpolated NWM values, which are usually used to detect major issues, discontinuities, outliers, etc. Thus, conclusions of intra-algorithms superiority will be reserved for the next comparisons.

Among the three observatories, SGP showed the largest amplitude of the differences (Table 10), as well as a strong seasonal signal (Figure 16). This result is in agreement with Figure 7 which presents the annual amplitude of WTC_{NWM} for the entire globe. In Figure 7, SGP, conversely to ENA and OLI, is located in a region with a large amplitude of the WTC seasonal signal, and therefore, the higher WTC differences for this observatory may be due to the low capacity of ERA5 to modulate this large seasonal variability. Additionally, the WTC_{NWM} variability categorization - Table 6 (previously provided for all observatories in subchapter 3.4), reinforces the strong seasonal signal, showing the large WTC variability that reaches the SGP region, with an annual mean of 13.57 cm and StD, which represents the variability, of 8.54 cm.

On the other hand, a weak seasonal signal is observed for the ENA observatory (Figure 14), which is reinforced by WTC_{NWM} variability categorization - Table 6. Table 6 shows that, while the ENA region has a high annual WTC mean of 14.6 cm, the WTC annual variability is smaller, represented by a StD of 5.3 cm.

The OLI observatory had the smallest amplitude of the differences, accompanied by a strong seasonal signal. Again, Table 6 reinforces this results by showing a small annual WTC Mean of 5.56 cm and a StD, of the same magnitude order, of 4.15 cm. This may indicate that the variations that occur in this region can be expressive as the season changes.

Looking only to the annual WTC Mean of the three observatories (Table 6), it can be seen that these values are possibly related to the RMS of the differences for the present comparison (WTC_{GB}, WTC_{NWM}) (Table 8 - Table 10). Therefore, the low annual Mean of the WTC for the OLI observatory (5.56 cm), probably due to the low temperatures, reflect in the good RMS accuracy of 0.56 cm and 0.50 cm, for the NN and MWRRETV2 respectively. Conversely, for the OLI and SGP observatories, the RMS of the WTC differences above 1.0 cm may be due to the higher annual Mean WTC (13.57 cm and 14.62 cm respectively) reached in these regions, probably due to the higher temperatures.

Thus, in this comparison with the NWM (WTC_{GB}, WTC_{NWM}), the seasonal signal of the RMS of the differences will depend on how the variability of the WTC occurs at a particular location. This is linked to the fact that, in seasons of high water vapour variability, the interpolated values from the ERA5 model cannot estimate the WTC_{NWM} very accurately, and therefore these will distance themselves from the values measured by the MWR_{GB}.

4.3 *Comparison with on-board Microwave Radiometers*

This section presents the comparison between the WTC from the ground-based radiometers and those from the MWR on board Sentinel-3A, Sentinel-3B, SARAL/Altica and Jason-3. This comparison (WTC_{GB}, WTC_{OB}) was performed for the ENA and OLI observatories. For each observatory, the RMS of the WTC differences (for the two ARM algorithms) and the corresponding WTC from the MWR aboard each altimeter mission are represented graphically in Figure 17 - Figure 23. Each figure is followed by a table with the number of samples analysed per class of distance to each observatory (Table 11 - Table 17).

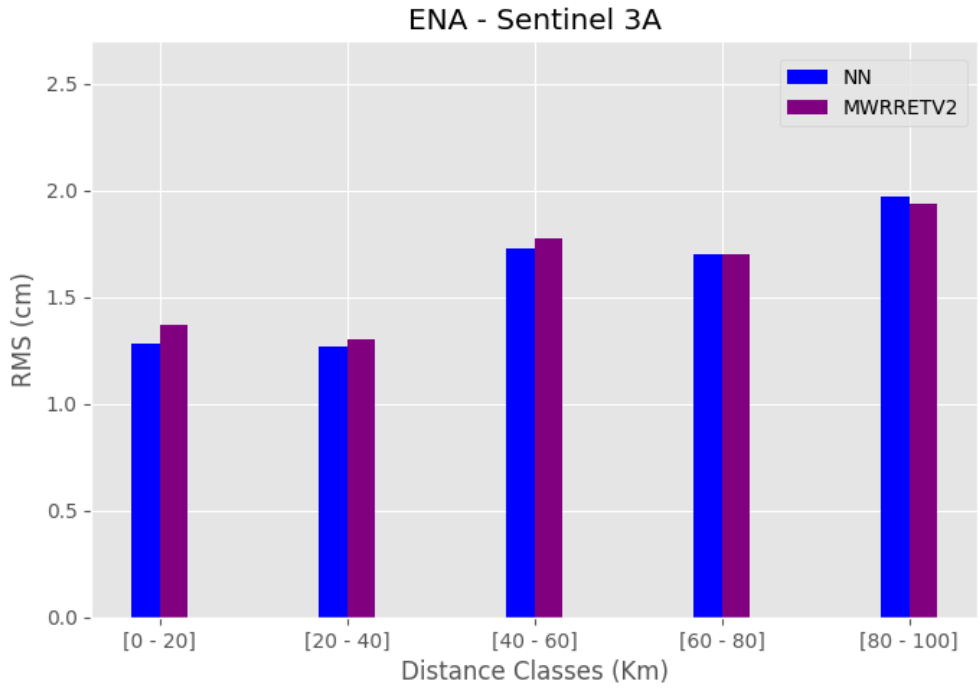

Figure 17 - RMS of the WTC differences between the products of the ARM algorithms and the Sentinel 3A on-board MWR, for the ENA observatory. The differences were computed for 5 classes of distance to the ENA Observatory.

Table 11 - Number of samples, per class, which is the same for both NN and MWRRETV2 algorithm assessment. This table refers to the results shown in Figure 17.

Classes (km)	**[0 - 20]**	**[20 - 40]**	**[40 - 60]**	**[60 - 80]**	**[80 - 100]**
Samples	10	362	297	1,183	1,776

Figure 17 presents the RMS values of the differences between the WTC_{GB} from the ENA observatory and WTC_{OB} from Sentinel 3A. This figure shows that the RMS of the WTC differences have a general tendency to increase as the distance class increases. The smallest RMS were observed in the class [20 - 40 km], with 1.27 cm and 1.30 cm for the NN and MWRRETV2 algorithms respectively. Table 11 indicates that the class [0 - 20 km] obtained only 10 samples, and therefore, strong conclusions cannot not be drawn for this class. The longest distance class [80 - 100 km] obtained the highest RMS values, of 1.97 cm and 1.93 cm for the NN and MWRRETV2 algorithms respectively.

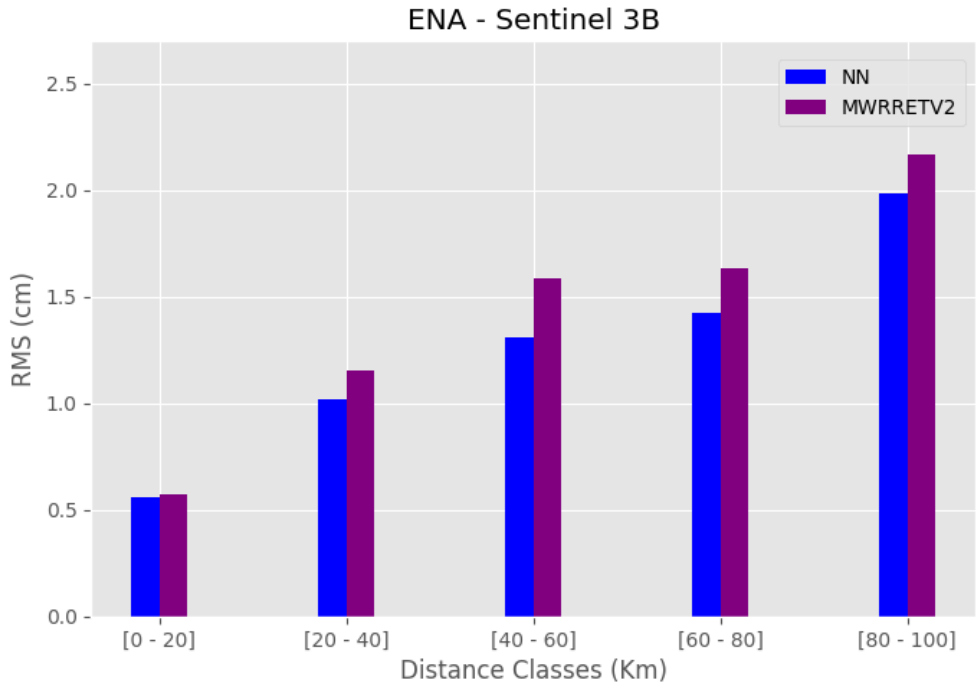

Figure 18 - RMS of the WTC differences between the products of the ARM algorithms and the Sentinel 3B on-board MWR, for the ENA observatory. The differences were performed for 5 classes of distance to the ENA Observatory.

Table 12 – Number of samples, per class, which is the same for both NN and MWRRETV2 algorithm assessments. This table refers to the results shown in Figure 18.

Classes (km)	**[0 - 20]**	**[20 - 40]**	**[40 - 60]**	**[60 - 80]**	**[80 - 100]**
Samples	6	356	576	528	613

The RMS of the differences between the WTC_{GB} from ENA observatory and WTC_{OB} from Sentinel-3 B is in Figure 18. These results show an increase in the RMS as the distance between classes increases. All classes showed a better performance of the NN algorithm over MWRRETV2. For example, the largest intra-algorithm difference occurred for the class [40 - 60 km], in which the NN algorithm obtained an RMS of 1.31 cm versus 1.59 cm for MWRRETV2.

Also for this result, no strong conclusions can be drawn for the class [0 - 20 km] due to the small number of 6 samples (Table 12). The RMS values for the class [20 - 40 km] were 1.02 cm and 1.16 cm for the NN and MWRRETV2 algorithms respectively. Furthermore, the longest distance class [80 - 100] showed the highest RMS values, with 1.98 cm for NN and 2.1 cm for MWRRETV2.

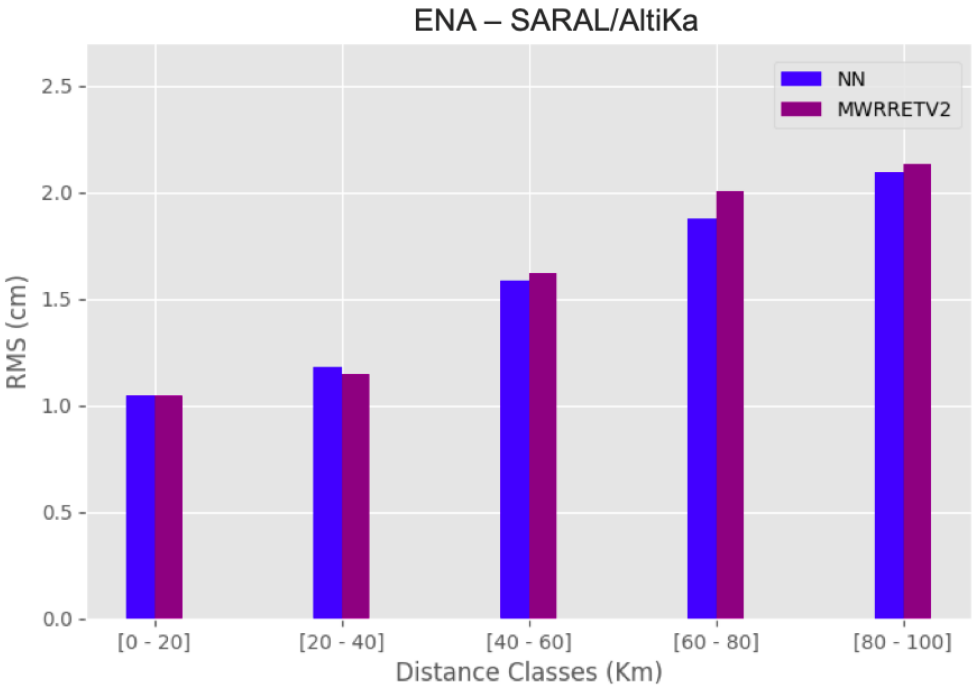

Figure 19 - RMS of the WTC differences between the products of the ARM algorithms and the SARAL/AltiKa on-board MWR, for the ENA observatory. The differences were performed for 5 classes of distance to the ENA Observatory.

Table 13 - Number of samples, per class, which is the same for both NN and MWRRETV2 algorithm assessments. This table refers to the results shown in Figure 19.

Classes (km)	**[0 - 20]**	**[20 - 40]**	**[40 - 60]**	**[60 - 80]**	**[80 - 100]**
Samples	276	992	1,587	1,963	2,733

Figure 19 presents the RMS of the differences between the WTC_{GB} from the ENA observatory and WTC_{OB} from SARAL. Also for this validation, the RMS values increase with distance. The class [0 - 20 km] demonstrated the lowest RMS values, as well as the smallest intra-algorithm RMS difference, since both NN and MWRRETV2 algorithms obtained the same RMS of 1.04 cm. The class [20 - 40 km] obtained slightly higher RMS values compared to the previous class, of 1.18 cm for NN and 1.15 for MWRRETV2. The last two classes [60 - 80 km] and [80 - 100 km] showed RMS accuracies of 1.88 cm and 2.0 cm for the NN algorithm respectively, and 2.10 and 2.13 cm for the MWRRETV2 algorithm respectively.

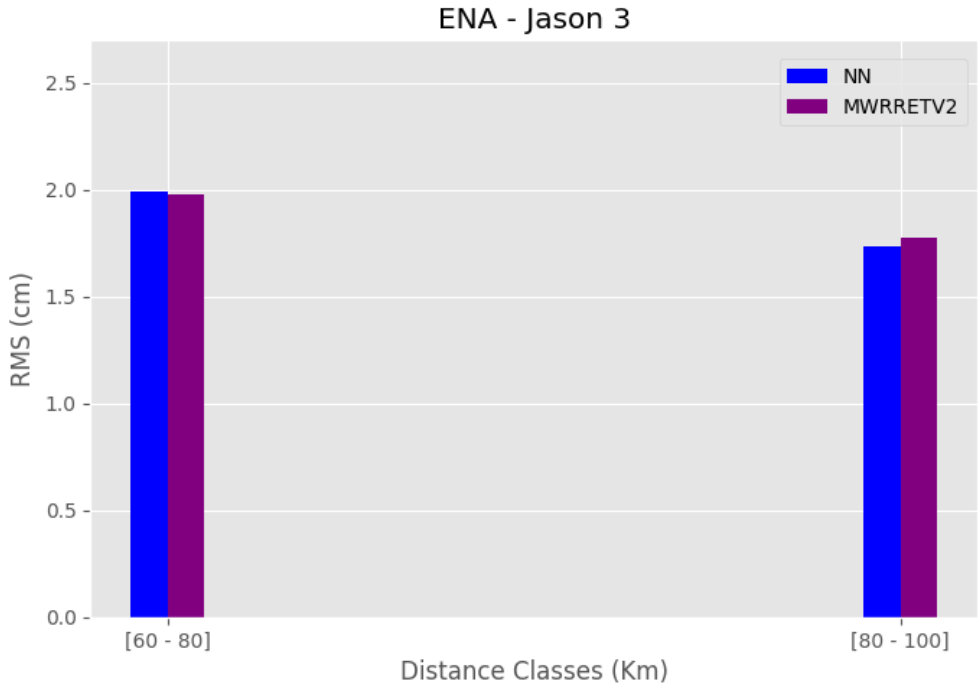

Figure 20 - RMS of the WTC differences between the products of the ARM algorithms and the Jason-3 on-board MWR, for the ENA observatory. The differences were performed for 2 classes of distance to the ENA Observatory.

Table 14 – Number of samples, per class, which is the same for both NN and MWRRETV2 algorithm assessments. This table refers to the results shown in Figure 20.

Classes (km)	**[60 - 80]**	**[80 - 100]**
Samples	15	2,706

The RMS of the differences between the WTC_{GB} from the ENA observatory and WTC_{OB} from Jason-3 is in Figure 20. In this validation, only WTC_{GB} measurements for the two most distant classes were found. In fact, the class [60 - 80 km] presented only 15 samples (Table 14), so no strong conclusions can be drawn for this class. On the other hand, the class [80 - 100 km], which obtained 2,706 samples, showed a slightly smaller RMS value for the NN algorithm, of 1.73 cm, when compared to the RMS obtained by MWRRETV2, of 1.77 cm. In addition, the RMS values for the [80 - 100 km] class were the lowest when compared to the same class for all other missions.

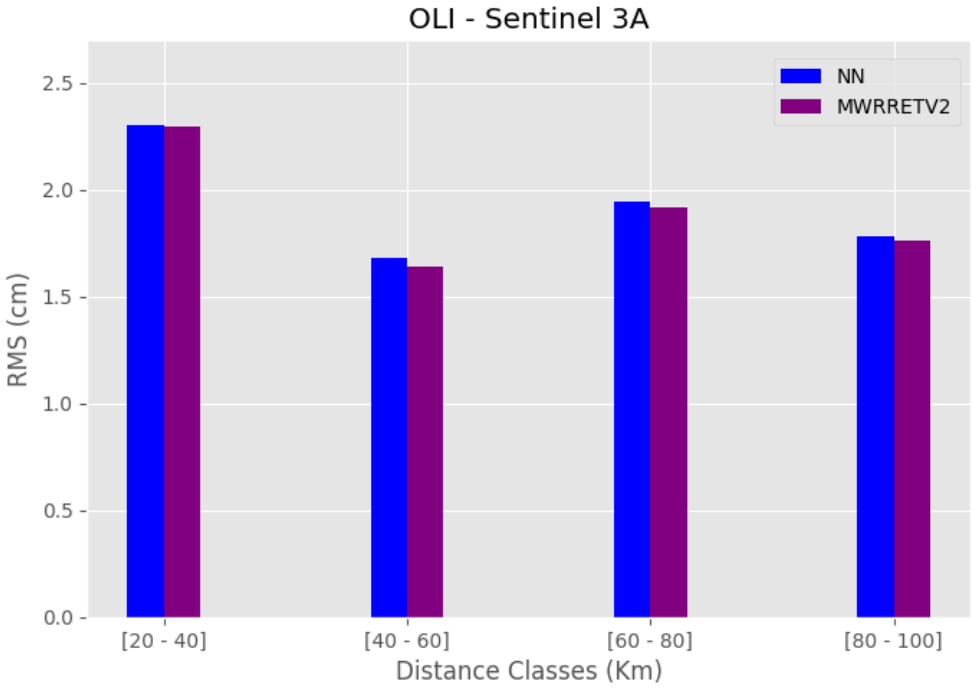

Figure 21 - RMS of the WTC differences between the products of the ARM algorithms and the Sentinel 3A on-board MWR, for the OLI observatory. The differences were computed for 4 classes of distance to the OLI Observatory.

Table 15 – Number of samples, per class, which is the same for both NN and MWRRETV2 algorithm assessments. This table refers to the results shown in Figure 21.

Classes (km)	**[20 - 40]**	**[40 - 60]**	**[60 - 80]**	**[80 - 100]**
Samples	103	293	335	607

Figure 21 presents the RMS of the differences between the WTC_{GB} from the OLI observatory and WTC_{OB} from Sentinel 3A. The nearest distance class [20 - 40 km] showed the highest WTC differences, in which both NN and MWRRETV2 algorithms obtained the RMS of approximately 2.30 cm. The class [40 - 60 km] obtained the lowest RMS in this evaluation, of 1.68 cm for NN and 1.64 for MWRRETV2.

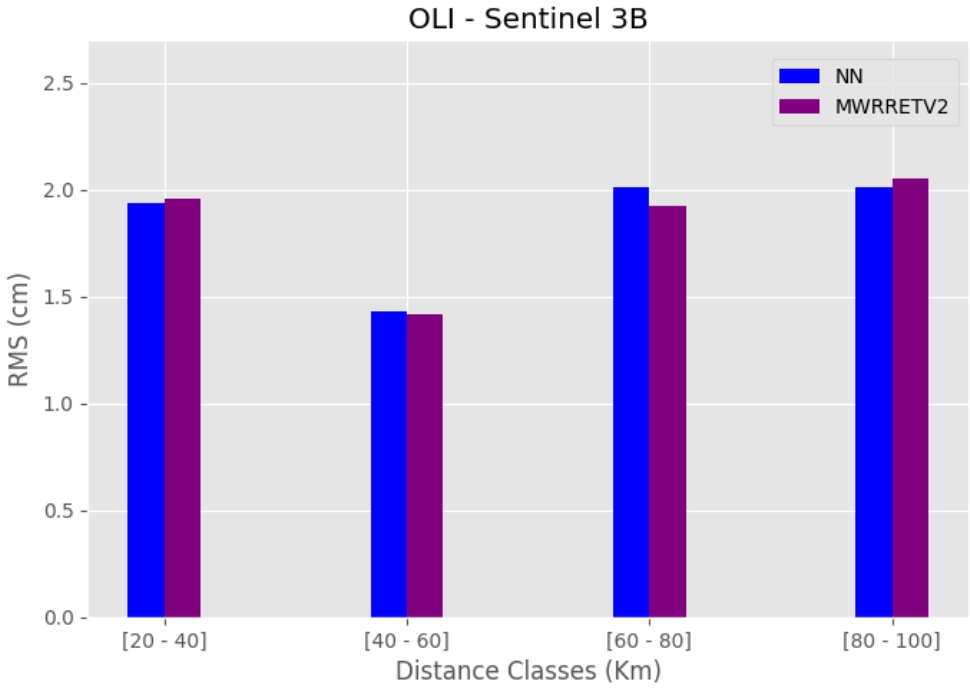

Figure 22 - RMS of the WTC differences between the products of the ARM algorithms and the Sentinel 3B on-board MWR, for the OLI observatory. The differences were performed for 4 classes of distance to the OLI Observatory.

Table 16 – Number of samples, per class, which is the same for both NN and MWRRETV2 algorithm assessments. This table refers to the results shown in Figure 22.

Classes (km)	**[20 - 40]**	**[40 - 60]**	**[60 - 80]**	**[80 - 100]**
Samples	32	85	136	213

The RMS of the differences between the WTC_{GB} from the OLI observatory and WTC_{OB} from Sentinel 3B is in Figure 22. In this evaluation, except for the class [20 - 40 km], the RMS values increase as the distance to OLI observatory increases. The class [20 - 40 km] obtained RMS of 1.94 cm for NN and 1.96 for MWRRETV2. The class [40 - 60 km] obtained decreased RMS values compared to the previous class, of 1.43 cm for NN and 1.41 for MWRRETV2. All intra-algorithmic comparisons showed a great similarity in the RMS values for all classes, however the class [60 - 80 km] showed a slightly better performance of the MWRRETV2 algorithm compared to NN.

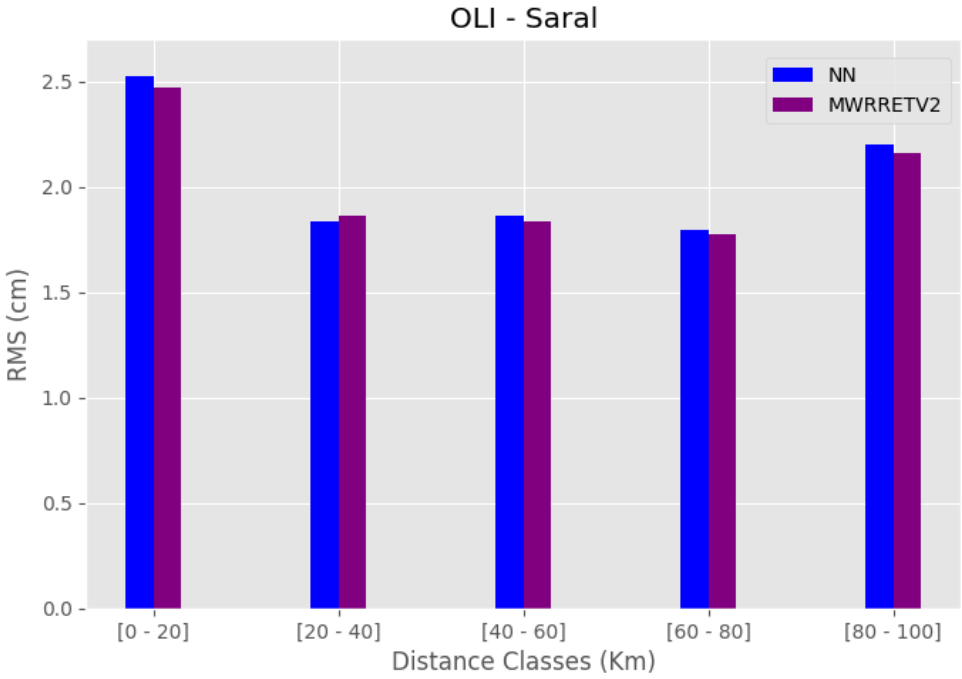

Figure 23 - RMS of the WTC differences between the products of the ARM algorithms and the SARAL on-board MWR, for the OLI observatory. The differences were performed for 5 classes of distance to the OLI Observatory.

Table 17 – Number of samples, per class, which is the same for both NN and MWRRETV2 algorithm assessments. This table refers to the results shown in Figure 23.

Classes (km)	**[0 - 20]**	**[20 - 40]**	**[40 - 60]**	**[60 - 80]**	**[80 - 100]**
Samples	63	186	337	533	675

The RMS of the differences between the WTC_{GB} from the OLI observatory and WTC_{OB} from SARAL is in Figure 23. This was the only evaluation for the OLI observatory in which there were WTC_{OB} measurements in the class [0 - 20 km]. The RMS values for the class [0 - 20 km] were much higher than the other distance classes, in which both the NN and MWRRETV2 algorithms obtained 2.53 cm and 2.47 cm respectively. The classes [20 - 40 km], [40 - 60 km], and [60 - 80 km] obtained very similar RMS values, which were respectively (for NN and MWRRETV2 respectively): 1.84 cm and 1.87 cm; 1.87 cm and 1.84 cm; 1.80 cm and 1.78 cm. The class [80 - 100 km] presented the highest RMS values, of 2.20 cm for the NN and 2.16 cm for MWRRETV2.

- *Discussion*

The graphical results for the ENA observatory (Figure 17 - Figure 20) showed that, in general, the WTC differences between the MWR_{GB} and MWR_{OB} instruments increased as the distance from the observatories increased. Thus, the high variability of water vapour is demonstrated in accordance with the increasing non-collocation spatial effect between measurements. The Sentinel-3 A and B and SARAL missions obtained valid WTC_{GB} measurements in the class [0 - 20 km], and therefore RMS values have been graphically represented. However, due to the large amount of land-contaminated measurements

which were previously rejected in this analysis, both Sentinel missions showed very low sample numbers (10 and 6) in this closest distance class (Table 11 and Table 12).

On the other hand, the SARAL mission showed an expressively more significant number of samples in the class [0 - 20 km] – 276 (Table 13), indicating then a lower rejection of ground-contaminated WTC_{OB} measurements. This higher number may be due to the facts that, the SARAL mission orbits at lower altitudes and both MWR_{OB} and altimeter instruments share the same antenna. Therefore, in addition to allowing measurements to be perfectly collocated between both equipment, both facts result in lower footprints of 8 - 12 km (depending on the channel frequency). Hence, SARAL MWR_{OB} shows less contaminated measurements up to 15 km from the coast or sea ice, compared to the other MWR_{OB} dual channel instruments [18,77]. Another possibility is that, due to technical problems, the SARAL current status of "orbit-drift" prevents the satellite from revisiting the same locations during each cycle [59], causing SARAL to take measurements at more locations than expected (see Figure 9 – bottom right).

Fortunately, the significant number of samples achieved in the class [0 - 20 km], with SARAL, allowed conclusions to be drawn for the class with the lowest non-collocation effect. Thus, the RMS values for this class were very close to 1.0 cm for both algorithms (Figure 19), indicating an agreement of this result with the previous comparison (WTC_{GB}, WTC_{NWM}) (1.09 cm – 1.19 cm) (Table 8). Additionally, the class [20 - 40 km] showed slightly higher RMS values (1.15 cm – 1.18 cm) than the previous class [0 - 20 km], which is probably due to the increased effect of non-collocation for this class.

Still for the same observatory, it is observed that the results found in the comparison with WTC_{OB} from the Jason-3 mission were graphically demonstrated only for the classes [60 - 80 km] and [80 - 100 km] (see Figure 9 – top), in spite of the fact that the class [60 - 80 km] obtained too low number of samples to be drawn realistic conclusions. However, the farthest distant class [80 - 100 km] showed the lowest RMS values when compared to the same class from the other missions. Considering that the spatial non-collocation effect is the same for this class [80 - 100 km] in all ENA observatory comparisons, the better agreement between the WTC_{GB} values and the WTC_{OB} values can be justified due to the presence of the lower frequency band - 18 GHz - in the Jason-3 MWR_{OB}. Thus, the information obtained due to the inclusion of a low frequency channel may be more effective in WTC_{OB} retrieval algorithms than the altimeter-derived wind speed or the backscatter coefficient information, which are used in the Sentinel-3 A/B and SARAL/AltiKa missions. For stronger conclusions, analyses with closer MWR_{GB} measurements would be needed, since the class [80 - 100 km] is at the limit of the WTC spatial correlation scale [71], and therefore caution should be taken when analysing these results.

As expected, in most of the comparisons for both observatories, the number of samples are larger as the distance classes increase. This is because increasing distance ranges lead to larger WTC_{OB} data collection areas, as well as the pollution of WTC_{OB} measurements is lower due to the increased distance from the Coastal Zone. For the comparisons at the ENA observatory this trend is not observed for the Sentinel-3 A and B missions, due to the Azores being formed by a complex of islands (Figure 9). Thus, as the distance classes increase, some collection areas overlap land regions, resulting in a large rejection of WTC_{OB} contaminated by land. In contrast, for the OLI observatory, the number of samples in all comparisons showed the expected increasing trend.

The graphical results for the OLI observatory did not show the increasing behaviour of RMS of the differences as the distance from MWR_{GB} increased (Figure 21 - Figure 23). For the Sentinel-3 A/B and SARAL/AltiKa missions comparisons, the classes [0 - 20 km] (SARAL only) and [20 - 40 km] exceeded 2.0

cm in most cases. This result disagrees with the previous comparison (WTC_{GB}, WTC_{NWM}), as well as with the results seen for the same comparison (WTC_{GB}, WTC_{OB}) of ENA Observatory. In contrast, the values found for the classes [40 - 60 km], [60 - 80 km], and [80 - 100 km] generally agree with the results seen for the same comparison (WTC_{GB}, WTC_{OB}) of ENA Observatory.

This anomaly observed, in the classes up to 40 km, may demonstrate a possible land contamination of the WTC_{OB} measurements, or even an ice contamination since the Arctic Ocean, which borders Northern Alaska, has high sea ice concentrations during most of the year [78]. Due to the previous rejection of measurements flagged as contaminated in this work, this hypothesis would indicate that possibly incorrect tracking of invalid on-board MWR measurements occurs for the Sentinel-3 A/B and SARAL/AltiKa missions. A previous study [79] had raised the need to improving the tracking of invalid Sentinel-3A MWR_{OB} measurements, since the authors observed the persistence of WTC_{OB} measurements contaminated by land and especially ice, even after the screening this measurements through quality flags. For the present study, an effective selection criteria would be to reject WTC_{OB} measurements that exceed a certain threshold in the difference with interpolated WTC from NWM (WTC_{NWM}), which will be applied in future works.

The intra-algorithm assessment showed that both NN and MWRRETV2 algorithms obtained similar results, including some cases of very similar RMS values, suggesting that the two algorithms have similar accuracies.

Finally, shortest distance classes to the ENA observatory, for which the number of observations is significant, represented the most consistent results of this comparison. Thus, at the ENA observatory, the comparisons with SARAL classes [0 - 20 km] and [20 - 40 km], and Sentinel-3 A/B class [20 - 40 km], show that the RMS of the WTC differences between the analysed ground-based radiometer and those from the on-board MWR range from 1.02 cm to 1.30 cm.

4.4 *Comparison with Radiosondes*

This subsection presents the comparison between the ground-based radiometers (MWR_{GB}) and radiosondes (WTC_{RS}) which were carried out for the ENA and SGP observatories, being the only not independent assessment in this study, since the information provided by this source is also introduced in the NN and MWRRETV2 algorithms. For the ENA observatory there is one RS (LAJES) at 89 km distance while for the SGP site there is one RS (LAMONT) at only 1.5 km distance.

The graphical results of this subsection are demonstrated through Figure 24 and Figure 25. These figures show the time series of the differences between the WTC_{GB} values of the two algorithms provided by ARM compared to the WTC_{RS} values. Although there is a low frequency of differences outside the limits shown on the y-axis [10 cm, -10 cm], this representation allows the behaviour of the differences to be plotted with better resolution. Additionally, a linear fit of the differences was inserted in all results. The statistics previously proposed in this work were also presented in Table 18 and Table 19. These tables include the maximum and minimum values of the differences which were suppressed by the charts.

Figure 24 represents the differences computed for the ENA observatory with a spatial non-collocation of 89 km. The charts for both results show that the dispersion of the differences has similar patterns. Furthermore, the trend line (red) demonstrates the occurrence of a positive slope over the analysed time series.

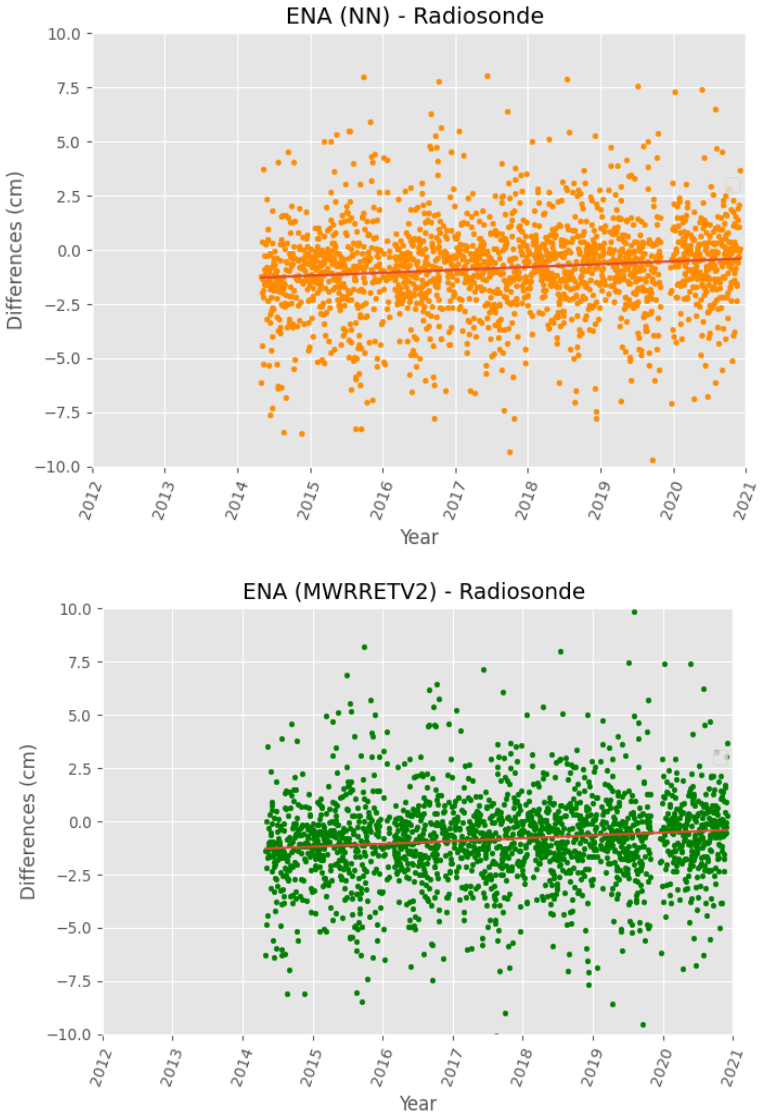

Figure 24 - WTC differences between the products of the radiosonde and ARM algorithms for the ENA observatory - NN (top) and MWRRETV2 (bottom).

The global statistics parameters for the ENA observatory (Table 18) showed that both algorithms achieved very similar performances, with approximately 2.20 cm and 2.37 cm for the StD and RMS statistics respectively. The Mean of the differences, in absolute value, for the MWRRETV2 algorithm was very similar.

Table 18 - Global statistics of the WTC difference between the products of the ARM algorithms and the radiosonde, for the ENA observatory.

	Samples	Mean (cm)	StD (cm)	RMS (cm)	Min (cm)	Max (cm)
NN	1,976	-0.84	2.22	2.37	-11.94	12.30
MWRRETV2		-0.90	2.19	2.36	-11.97	12.18

The WTC differences for the SGP observatory are shown in Figure 25. For this observatory, the compared measurements are approximately 1.5 km apart. As evaluated before, the dispersion of the differences is similar for both algorithms. However, it is observed that the differences for the MWRRETV2 algorithm showed a higher frequency of difference values above 5 cm in absolute value. Also for this observatory, the trend line (red) showed that this comparison has a positive slope for the differences in the analysed time series.

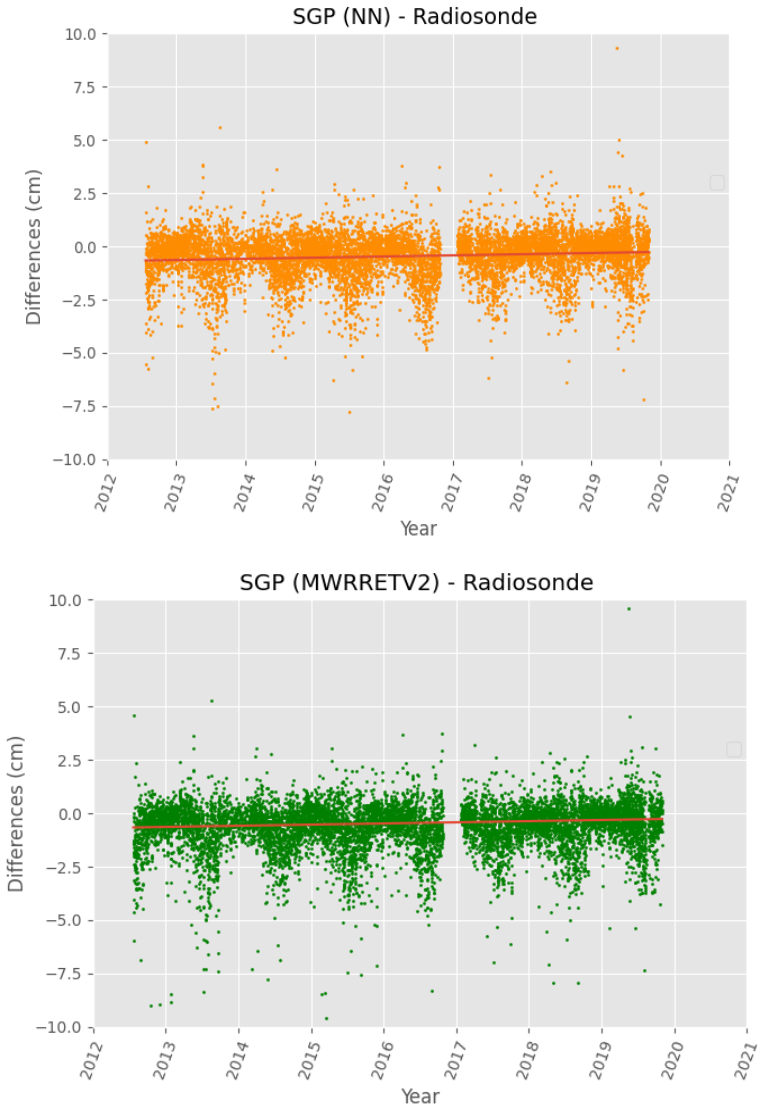

Figure 25 - WTC differences between the products of the ARM and radiosonde algorithms for the SGP observatory - NN (top) and MWRRETV2 (bottom).

Despite the graphical similarity of the differences (Figure 25), the overall statistics (Table 19) showed that the NN algorithm had better performance than MWRRETV2. In this comparison, the difference statistics of the NN algorithm showed absolute values of Mean, StD, and RMS which were lower by approximately 0.27 cm, 0.58 cm, and 0.59 cm respectively.

Table 19 – Global statistics of the WTC differences between the products of the ARM algorithms and the radiosonde, for the SGP observatory.

	Samples	Mean (cm)	StD (cm)	RMS (cm)	Min (cm)	Max (cm)
NN	9,296	-0.46	1.18	1.26	-21.89	9.32
MWRRETV2		-0.74	1.70	1.86	-24.99	9.57

- *Discussion*

The results of the differences represented graphically for both the ENA and SGP observatories (Figure 24 - Figure 25) showed a slightly positive slope (all below 0.02 mm/yr) in the presented time series. Therefore, even if this trend is minor, it is observed that as time increases the IGRA WTC_{RS} tends to have higher values than the WTC_{GB}.

The RMS statistics for the ENA observatory showed values close to 2.38 cm for both algorithms. Since the measurements in this comparison are non-collocated at approximately 89 km, the accuracy found is in agreement with the results in the previous comparison (WTC_{GB}, WTC_{OB}), where the farthest classes for the Sentinel-3 A/B and SARAL/AltiKa missions showed RMS in the same order of magnitude (from 1.93 cm to 2.13 cm) (Figure 17 - Figure 20). Again, the conclusions at these distances must be carefully analysed, as they are at the limit of the WTC spatial correlation scale [71].

For the SGP observatory, in which spatial collocated WTC_{RS} measurements were used (1.5 km apart), the NN algorithm obtained a better accuracy of 1.27 cm, which is in agreement with the results found in the classes up to 40 km of the comparison with MWR_{OB} (WTC_{GB}, WTC_{OB}). On the other hand, the MWRRETV2 algorithm showed a lower RMS accuracy of 1.86 cm. Thus, as this comparison with RS is a not independent assessment, this intra-algorithm difference of approximately 6.0 mm may indicate that RS information has a greater contribution in the construction of the NN algorithm than in the MWRRETV2 algorithm

4.5 *Comparison with GNSS*

This section presents the comparison between the WTC from the ground-based radiometers and GNSS-derived WTC. Results are presented both for the NN algorithm and for the two newly developed algorithms in the scope of this thesis. Therefore, RMS of the differences are presented in Figure 26, as well as the statistics parameters in Table 20.

Only the ENA observatory produced results in the comparison (WTC_{GB}, WTC_{GNSS}), since an IGS GNSS station (ENAO) was found 51 m away and with data availability of more than 1 year (Table 4). Although for the OLI observatory no GNSS data have been found at a distance of up to 100 km, for SGP observatory, a GNSS station of the IGS network was found nearby. However, the temporal compatibility with both ARM algorithms (NN and MWRRETV) was too low to conduct comparisons.

For ENA, the comparison (WTC_{GB}, WTC_{GNSS}) was carried out only with the NN algorithm, since only for this algorithm were data available for a period of more than one year (approximately 15 months). Indeed, a comparison with both algorithms was possible for a period of 10 months. However, no

significant conclusions could be drawn, due to the short period under analysis that does not consider the full representation of the annual variability of WTC. Therefore, these results were not considered relevant for this study.

As mentioned above, a new neural network algorithm was trained aiming to estimate the WTC directly from the TB observed by the ground-based MWR channels. For that, WTC from NWM were used as output in the train dataset. Two versions of the algorithm were created: (1) using 2 inputs - TB from both 23.8 and 30 GHz channels (henceforth called WTC_{GB_2TB}); and (2), using 3 inputs - inclusion of the TB from the 90 GHz channel (henceforth called WTC_{GB_3TB}). Thus, the results of the comparisons with both WTC_{GB_2TB} and WTC_{GB_3TB} algorithms and GNSS are also presented in this subsection.

In Figure 26, the NN algorithm demonstrated the higher RMS of the differences of 1.41 cm. Regarding the novel algorithms developed in this study, the 3 inputs version (WTC_{GB_3TB}) had slightly better RMS of the differences of 1.34 cm than the 2 inputs version (WTC_{GB_2TB}) which presented 1.42 cm of RMS.

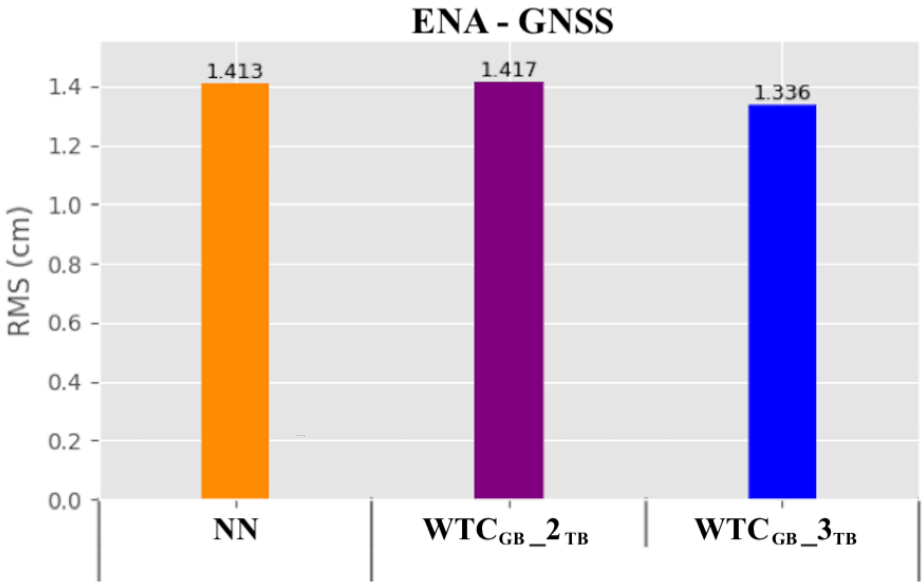

Figure 26 - RMS of the WTC difference of NN, WTC_{GB_2TB} and, WTC_{GB_3TB} algorithms relative to the GNSS data, for the ENA observatory. The data period collected is approximately 15 consecutive months

Table 20 shows that the Mean statistics for the NN algorithm had the lowest absolute value of 0.26 cm while the WTC_{GB_3TB} had the highest value, of 0.33 cm. The NN and WTC_{GB_2TB} recorded the same StD statistic, obtaining both a value of approximately 1.39 cm. The WTC_{GB_3TB} recorded the lowest value of the StD statistics, at approximately 1.30 cm.

Table 20 – Global statistics parameters of the WTC differences of NN, WTC_{GB_2TB} and, WTC_{GB_3TB} algorithms relative to the GNSS data, for the ENA observatory.

	Samples	Mean (cm)	StD (cm)	Min (cm)	Max (cm)
NN	42,052	-0.261	1.389	-9.818	6.099
WTC_{GB_2TB}		0.277	1.389	-8.119	16.280
WTC_{GB_3TB}		0.322	1.296	-8.179	16.110

- *Discussion*

Due to the recent availability of ZTDs by IGS for the ENAO GNSS station, a period of approximately 15 months of data was used for the comparison. In addition, data from the MWRRETV2 algorithm for 2021 has not yet been made available by ARM - at the present date of this work, making a temporal correlation better than 10 months impossible. Hopefully, new data will soon be available from both interdependent sources, in order to obtain results in future work.

The NN algorithm showed a RMS of 1.41 cm (Figure 26) which is in agreement with other previous comparisons for the ENA observatory, such as the comparison with MWR_{OB} - classes up to 40 km for all mission (1.02 cm - 1.30 cm.) and the comparison with NWM (1.09 cm - 1.19cm).

The WTC_{GB_3TB} showed a better accuracy when compared with the WTC_{GB_2TB}, in spite of the RMS differences between both versions being in sub millimetre scale. Therefore, information from the 89 GHz band of the MWR_{GB} - which is intended to detect lower amounts of precipitable water vapor (TCWV < 5 mm), proved to be an information with a positive contribution to the algorithm's retrieval.

Additionally, the WTC_{GB_3TB} presented a better accuracy than the NN algorithm. This better performance of the WTC_{GB_3TB} algorithm may be due to the direct deduction of WTC_{GB} values from MWR_{GB} TB, whereas the retrieval of WTC_{GB} values from ARM algorithms required at least 2 intermediate steps: (1st) deducing TCWV values from the Brightness Temperatures via the NN or MWRRETV2 algorithm; and (2nd) converting TCWV to WTC_{GB} with Equation (3). Therefore, the errors underlying these steps may have been overcome by using the WTC_{GB_3TB}.

5. Conclusion

This study exploited the ground-based radiometers (MWR_{GB}) in the context of Satellite Altimetry, based on the well-established acquisition of total column water vapour (TCWV) measurements by this equipment. Additionally, MWR_{GB} have not yet been exploited in the context of Satellite Altimetry, and therefore, this research has the role of initiating a research into the accuracy of this equipment in obtaining WTC measurements from TCWV data. As addressed before, on-board MWR (MWR_{OB}) algorithms have issues in retrieving valid WTC_{OB} measurements over surface transition regions such as coastal zones, inland waters, and sea ice. Despite the existence of WTC sources that compensate this lack of valid measurements, such as NWM and GNSS, they are limited in accuracy for the former and in spatial resolution for the latter. Thus, the further use of reliable WTC measurements from MWR_{GB} (WTC_{GB}) can contribute as a new source for altimeter observations over transition zones - especially when there are no GNSS stations in the region - and for calibration and validation purposes. Moreover, Since MWR_{GB} and MWR_{OB} have brightness temperatures (TB) as their fundamental measurement, studies involving the collocated comparison between this variable of both equipment may be promising.

In the present work, observations from three ARM observatories have been analysed. These have been assessed by comparison with WTC from four external sources: ERA5 model, MWR on-board 4 altimeter missions (Sentonel-3A, Sentinel-3B, SARAL and Jason-3), Radiosondes (RS) and GNSS.

Among the three analysed observatories, only the ENA site obtained enough data from external sources to perform all 4 comparisons. In contrast, the OLI and SGP observatories produced results with only 2 comparisons. For the former, analyses were performed with WTC_{OB} and WTC_{NWM} data, and for the latter with WTC_{RS} and WTC_{NWM} data. All comparisons were carried out in parallel for the data retrieved from both ARM algorithms, which enabled an intra-algorithm evaluation.

The temporal collocation between measurements is guaranteed by the fact that ARM's MWR_{GB} has a fine temporal resolution of approximately 3 - 15 seconds, which has been resampled in this work to samples every 3 minutes. The spatial collocations in this work were up to a maximum of 100 km, which varied between the comparisons. Despite the decrease in RMS accuracy as the non-collocation between measurements increases, this variant was taken as an advantage to find concordances between the comparisons.

For the ENA observatory, the collocated and up to 40 km assessments showed very similar RMS values, which were (for NN and MWRRETV algorithms respectively): comparison with NWM (1.2 cm , 1.1 cm); comparison with MWR_{OB} for SARAL class [0 - 20 Km] (1.04 cm both); comparison with MWR_{OB} for SARAL class [20 - 40 km] (1.18 cm and 1.15 cm); comparison with MWR_{OB} for Sentinel-3 A class [20 - 40 km] (1.27 cm and 1.30 cm); comparison with MWR_{OB} for Sentinel-3 B class [20 - 40 km] (1.02 cm and 1.16 cm); and comparison with GNSS (1.41 cm for NN only).

For this same observatory, another RMS agreement was observed for non-collocated assessments in the 80 - 100 Km distance range, which were (for NN and MWRRETV algorithms respectively): comparison with Radiosonde (2.37 cm both); comparison with MWR_{OB} for SARAL class [80 - 100 Km] (2.0 m and 2.13 cm); comparison with MWR_{OB} for Sentinel-3 A class [80 - 100 Km] (1.97 cm and 1.93 cm); and comparison with MWR_{OB} for Sentinel-3 B class [80 - 100 Km] (1.98 cm and 2.1 cm).

For the OLI observatory, the RMS of the WTC differences for the comparison (WTC_{GB}, WTC_{NWM}) showed low values of 0.56 cm for NN and 0.50 cm for MWRRETV2. These results had no agreement with

the observed RMS values for the classes up to 40 km from the comparison with MWR_{OB} for the same observatory, which were (for the NN and MWRRETV algorithms respectively): comparison with MWR_{OB} for SARAL class [0 - 20 Km] (2.53 cm and 2.47 cm); comparison with MWR_{OB} for SARAL class [20 - 40 km] (1.84 cm and 1.87 cm); comparison with MWR_{OB} for Sentinel-3 A class [20 - 40 km] (2.30 cm both); and comparison with MWR_{OB} for Sentinel-3 B class [20 - 40 km] (1.94 cm and 1.96 cm). Perhaps, the WTC_{OB} for these classes were contaminated by sea ice or land and have not been excluded even with the previous rejection of measurements flagged as invalid. In this case, they are in agreement with results found in [6]. For differences between WTC_{OB} and WTC_{GNSS}, the authors achieved an RMS of the WTC differences above 1.60 cm in classes up to 25 km with contaminated WTC_{OB} measurements. Thus, in order to obtain only valid WTC_{OB} measurements, for future works a criteria will be implemented, for example, to reject the WTC_{OB} values that exceed a certain threshold in the difference with interpolated WTC_{NWM}.

For the SGP observatory, the RMS of the WTC differences for the comparison (WTC_{GB}, WTC_{NWM}) and the comparison (WTC_{GB}, WTC_{RS}) showed inverse agreement between the algorithms. While the former obtained RMS values of 1.89 cm for NN and 1.18 cm for MWRRETV2, the latter obtained RMS values of 1.27 cm for NN and 1.86 for MWRRETV2. Although this perhaps demonstrates an inconsistency of 6.0 - 7.0 cm, between the NN and MWRRETV2 algorithms, the results of the comparison with NWM cannot carry the same relevance as the results of the comparison with Radiosondes, since model values do not have the same accuracy as point measurements.

Still for the SGP observatory, a comparison with GNSS is envisaged, since there is a station from the IGS network producing collocated ZTD data since February 2020. In this work, the comparison (WTC_{GB}, WTC_{GNSS}) was not performed due to the advice from ARM to not use the available data in 2021 (subsection 3.1), which limited the temporal correlation between MWR and ground-based GNSS data.

Additionally, an assessment of the WTC directly retrieved from the TB observed by the ground-based MWR channels was carried out against WTC_{GNSS} data. For this, two novel neural network algorithms were developed exclusively for this work: (WTC_{GB_2TB}) using 2 inputs - TB from both 23.8 and 30 GHz channels; and (WTC_{GB_3TB}), using 3 inputs - inclusion of the TB from the 90 GHz channel. Both algorithms were tuned to derive WTC from the MWR_{GB} installed at the ENA observatory, based on interpolated WTC_{NWM} as training output.

The assessment of WTC_{GB_2TB} and WTC_{GB_3TB} algorithms, for the ENA observatory, showed an RMS accuracy of 1.42 and 1.34 cm respectively. Therefore, this small difference in accuracy is probably due to the introduction of information from the 90 GHz channel in the WTC_{GB_3TB}, in spite of the small difference, not significant to conclude which one is more accurate. Future research aims to perform comparisons of both algorithms tuned to derive WTC from the MWR_{GB} installed at OLI. Due to the 90 GHz channel being specific to detect small amounts of cloud liquid in the atmosphere, in extremely cold regions which have low water vapour content in the air, this frequency may have a more significant contribution to the retrieval accuracy of the WTC_{GB_3TB} algorithm relative to WTC_{GB_2TB}.

Furthermore, the RMS of the differences for the WTC_{GB_3TB} was lower than the RMS found in the same assessment of the NN algorithm (1.41 cm). This result demonstrates the valuable possibility in deducing WTC_{GB} data autonomously from MWR_{GB} TB observations. With this algorithm, it is expected that errors associated with the conversion steps from TB to WTC_{GB} are suppressed. Also, in future work, it is envisaged to evaluate this algorithm with other independent sources; as well as introduce different combinations of training outputs, such as GNSS and NWM, in order to observe better performances.

As a whole, this study showed interesting conclusions regarding the deduced WTC_{GB} from MWR_{GB} observations. The accuracy found for the ENA observatory, among the collocated assessments, showed close RMS values within a range of 1.02 cm - 1.41 cm. Therefore, these measurements proved to be very useful for correcting altimeter observations at a distance of up to 40 km. This equipment can also be used for independent assessments or even for the calibration and validation of other instruments.

The intra-algorithm assessment showed that in general the NN and MWRRETV2 algorithms have great similarity in their results, with RMS values in the range of 0 – 7.0 mm, in which only two assessments showed an intra-algorithm RMS difference of more than 2.8 mm. Therefore, for the needs of satellite altimetry, the NN algorithm proves to be a reliable source for deducing WTC_{GB}, due to the near real-time latency of its retrieved data.

Finally, assuming that measurements from ground-based microwave radiometer have proven to be a source for providing WTC for Satellite Altimetry, we (from the Satellite Altimetry Research Group) are looking forward to continuing studies with MWR_{GB}. One of the ideas that emerged, after this work, was to analyse MWR_{OB} contaminated TB through collocated comparison with MWR_{GB} valid TB. The former observation has the contribution of the atmosphere plus the surface in its brightness temperature while the latter observation has only the contribution of the atmosphere column (in both the cosmic background already compensated). Thus, through this comparison, it is expected to obtain a preliminary indicator about the surface contribution in the on-board radiometer TB. It is important to note that this comparison needs a careful analysis since it is dependent on various aspects, namely the distinct impact of the surface for different frequencies and the different frequencies used in the various sensors (on-board and ground-based).

Currently, collocated comparisons, up to 80 km, between MWR_{OB} contaminated TB with MWR_{GB} valid TB are being conducted. Preliminary results, for a single observatory (SGP), showed very systematic results for the Sentinel-3 A/B, SARAL and Jason-3 missions, in which all MWR_{OB} measurements were in a range of 0.9 - 0.99 of footprint land fraction. Next step is to cross-check all available data from existing MWR_{GB} observatories with on-board radiometer observations.

With this research, it is planned to examine the following points: (1) the contribution that non-open-ocean surfaces introduce to MWR_{OB} TB; (2) the correlation between the contribution introduced in (1) and the fraction of land/ice/snow/desert in the on-board radiometer footprint; and (3) the correlation between the contribution introduced in (1) and parameters such as the backscatter coefficient (sigma0), which concerns the interaction of the altimeter signal with different types of surfaces.

6. References

1. Pohl, C., & Van Genderen, J. L. (1998). Review article Multisensor image fusion in remote sensing: Concepts, methods and applications. International Journal of Remote Sensing, 19(5), 823–854.doi:10.1080/014311698215748

2. Fernandes, Maria; Lázaro, Clara (2018). Independent Assessment of Sentinel-3A Wet Tropospheric Correction over the Open and Coastal Ocean. Remote Sensing, 10(3), 484–. doi:10.3390/rs10030484

3. Fu, Lee-Lueng; Haines, Bruce J. (2013). The challenges in long-term altimetry calibration for addressing the problem of global sea level change. Advances in Space Research, 51(8), 1284–1300. doi:10.1016/j.asr.2012.06.005

4. Fernandes, M., Lázaro, C., Nunes, A., & Scharroo, R. (2014). Atmospheric Corrections for Altimetry Studies over Inland Water. Remote Sensing, 6(6), 4952–4997. doi:10.3390/rs6064952

5. N. Ducet; P. Y. Le Traon; G. Reverdin (2000). Global high-resolution mapping of ocean circulation from TOPEX/Poseidon and ERS-1 and -2. , 105(C8), 19477–19498. doi:10.1029/2000jc900063

6. Vieira, T., Fernandes, & M. J. Lazaro, C. (2018). Independent Assessment of On-Board Microwave Radiometer Measurements in Coastal Zones Using Tropospheric Delays From GNSS. IEEE Transactions on Geoscience and Remote Sensing, (), 1–13. doi:10.1109/TGRS.2018.2869258

7. Fernandes, M. J., Lázaro, C., & Vieira, T. (2021). On the role of the troposphere in satellite altimetry. Remote Sensing of Environment, 252, 112149.doi:10.1016/j.rse.2020.112149

8. Chelton, D. B., Ries, J. C., Haines, B. J., Fu, L.-L., & Callahan, P. S. (2001). Chapter 1 Satellite Altimetry. Satellite Altimetry and Earth Sciences - A Handbook of Techniques and Applications, 1–ii. doi:10.1016/s0074-6142(01)80146-7

9. Bertiger W, Desai S, Dorsey A, Haines B, Harvey N, Kuang D, Lane C, Weiss J, Sibores A (2008) Jason-2, Precision orbit determination status, OSTST workshop, Nice, Nov 2008, https://www.aviso.altimetry.fr/fileadmin/documents/OSTST/2008/Bertiger.pdf

10. Keihm, S.J.; Janssen, M.A.; Ruf, C.S. (1995). TOPEX/Poseidon microwave radiometer (TMR). III. Wet troposphere range correction algorithm and pre-launch error budget. , 33(1), 0–161. doi:10.1109/36.368213

11. Komjathy, A., & Born, G. H. (1999). GPS-based ionospheric corrections for single frequency radar altimetry. Journal of Atmospheric and Solar-Terrestrial Physics, 61(16), 1197–1203. doi:10.1016/s1364-6826(99)00051-6

12. Stum, J.; Sicard, P.; Carrere, L.; Lambin, J. (2011). Using Objective Analysis of Scanning Radiometer Measurements to Compute the Water Vapor Path Delay for Altimetry., 49(9), 3211–3224.doi:10.1109/tgrs.2011.2104967

13. Fernandes, M. J., Pires, N., Lázaro, C., & Nunes, A. L. (2013). Tropospheric delays from GNSS for application in coastal altimetry. Advances in Space Research, 51(8), 1352–1368.doi:10.1016/j.asr.2012.04.025

14. Pires, N., Fernandes, M. J., Gommenginger, C., & Scharroo, R. (2018). Improved Sea State Bias Estimation for Altimeter Reference Missions With Altimeter-Only Three-Parameter Models. IEEE Transactions on Geoscience and Remote Sensing, 1–15.doi:10.1109/tgrs.2018.2866773

15. Vieira, E., Lázaro, C., & Joana Fernandes, M. (2018). Spatio-temporal variability of the wet component of the troposphere – Application to Satellite Altimetry. Advances in Space Research.doi:10.1016/j.asr.2018.11.015

16. Karmakar, Pranab Kumar (2013). Ground-based microwave radiometry and remote sensing: Methods and applications. United States of America: CRC Press. Taylor & Francis Group. Version date: 2013916. doi: 10.1201/b15494.

17. Ruf, C. S., Keihm, S. J., Subramanya, B., & Janssen, M. A. (1994). TOPEX/POSEIDON microwave radiometer performance and in-flight calibration. Journal of Geophysical Research, 99(C12), 24915.doi:10.1029/94jc00717

18. Steunou, N., Picot, N., Sengenes, P., Noubel, J., & Frery, M. L. (2015). AltiKa Radiometer: Instrument Description and In–Flight Performance. Marine Geodesy, 38(sup1), 43–61. doi:10.1080/01490419.2015.1006381

19. Pacione, R., Pace, B., Vedel, H., de Haan, S., Lanotte, R., & Vespe, F. (2011). Combination methods of tropospheric time series. Advances in Space Research, 47(2), 323–335. doi:10.1016/j.asr.2010.07.021

20. Chen, B., & Liu, Z. (2016). Global water vapor variability and trend from the latest 36 year (1979 to 2014) data of ECMWF and NCEP reanalyses, radiosonde, GPS, and microwave satellite. Journal of Geophysical Research: Atmospheres, 121(19), 11,442–11,462. doi:10.1002/2016jd024917

21. Solheim, F., Godwin, J. R., Westwater, E. R., Han, Y., Keihm, S. J., Marsh, K., & Ware, R. (1998). Radiometric profiling of temperature, water vapor and cloud liquid water using various inversion methods. Radio Science, 33(2), 393–404.doi:10.1029/97rs03656

22. Askne, J., & Westwater, E. (1986). A Review of Ground-Based Remote Sensing of Temperature and Moisture by Passive Microwave Radiometers. IEEE Transactions on Geoscience and Remote Sensing, GE-24(3), 340–352.doi:10.1109/tgrs.1986.289591

23. Elgered, G., & Jarlemark, P. O. J. (1998). Ground-based microwave radiometry and long-term observations of atmospheric water vapor. Radio Science, 33(3), 707–717. doi:10.1029/98rs00488

24. Jassen, Michael A. (1937). Atmospheric Remote Sensing by Microwave Radiometry, United States of America: JOHN WILEY & SONS, INC. ISBN:0-471-62891-3.

25. Hosler, C. R., & Lemmons, T. J. (1972). Radiometric Measurements of Temperature Profiles in the Planetary Boundary Layer. Journal of Applied Meteorology, 11(2), 341–348. doi:10.1175/1520-0450(1972)011<0341:rmotpi>2.0.co;2

26. Decker, M. T., Westwater, E. R., & Guiraud, F. O. (1978). Experimental Evaluation of Ground-Based Microwave Radiometric Sensing of Atmospheric Temperature and Water Vapor Profiles. Journal of Applied Meteorology, 17(12), 1788–1795. doi:10.1175/1520-0450(1978)017<1788:eeogbm>2.0.co;2

27. Skoog, B. G., Askne, J. I. H., & Elgered, G. (1982). Experimental Determination of Water Vapor Profiles from Ground-Based Radiometer Measurements at 21.0 and 31.4 GHz. Journal of Applied Meteorology, 21(3), 394–400. doi:10.1175/1520-0450(1982)021<0394:edowvp>2.0.co;2

28. Westwater, E.R. (1965). Ground-Based Passive Probing Using the Microwave Spectrum of Oxygen. Radio Science, 69D(9), 1201. doi:10.6028/jres.069d.130

29. Elgered, G., Rönnäng, B. O., & Askne, J. I. H. (1982). Measurements of atmospheric water vapor with microwave radiometry. Radio Science, 17(5), 1258–1264. doi:10.1029/rs017i005p01258

30. Westwater, E. R. (1978). The accuracy of water vapor and cloud liquid determination by dual-frequency ground-based microwave radiometry. Radio Science, 13(4), 677–685. doi:10.1029/rs013i004p00677

31. Waters, J. W. (1976). 2.3. Absorption and Emission by Atmospheric Gases. Astrophysics - Radio Telescopes, 142–176. doi:10.1016/s0076-695x(08)60684-5

32. Cadeddu, M. P., Liljegren, J. C., & Pazmany, A. L. (2007). Measurements and Retrievals From a New 183-GHz Water-Vapor Radiometer in the Arctic. IEEE Transactions on Geoscience and Remote Sensing, 45(7), 2207–2215. doi:10.1109/tgrs.2006.888970

33. Cadeddu, M. P., Liljegren, J. C., & Turner, D. D. (2013). The Atmospheric radiation measurement (ARM) program network of microwave radiometers: instrumentation, data, and retrievals. Atmospheric Measurement Techniques, 6(9), 2359–2372. doi:10.5194/amt-6-2359-2013

34. Crewell, S., Ebell, K., Löhnert, U., & Turner, D. D. (2009). Can liquid water profiles be retrieved from passive microwave zenith observations? Geophysical Research Letters, 36(6). doi:10.1029/2008gl036934

35. Löhnert, U., & Crewell, S. (2003). Accuracy of cloud liquid water path from ground-based microwave radiometry 1. Dependency on cloud model statistics. Radio Science, 38(3), n/a–n/a. doi:10.1029/2002rs002654

36. Turner, D. D., Clough, S. A., Liljegren, J. C., Clothiaux, E. E., Cady-Pereira, K. E., & Gaustad, K. L. (2007). Retrieving Liquid Water Path and Precipitable Water Vapor From the Atmospheric Radiation Measurement (ARM) Microwave Radiometers. IEEE Transactions on Geoscience and Remote Sensing, 45(11), 3680–3690. doi:10.1109/tgrs.2007.903703

37. Mather, J. H., & Voyles, J. W. (2013). The Arm Climate Research Facility: A Review of Structure and Capabilities. Bulletin of the American Meteorological Society, 94(3), 377–392. doi:10.1175/bams-d-11-00218.1

38. Atmospheric Radiation Measurement (ARM) *user facility*. 2021. [Online]. https://www.arm.gov/. Accessed on: 04/08/2021.

39. Cadeddu, M. P., Turner, D. D., & Liljegren, J. C. (2009). A Neural Network for Real-Time Retrievals of PWV and LWP From Arctic Millimeter-Wave Ground-Based Observations. IEEE Transactions on Geoscience and Remote Sensing, 47(7), 1887–1900. doi:10.1109/tgrs.2009.2013205

40. Zhang D, L Riihimaki, KL Gaustad, and DD Turner. 2020. MWRRETV2 Value-Added Product Report: The Retrieval of Liquid Water Path and Precipitable Water Vapor from Microwave Radiometer – 3-Channel (MWR3C) Data Sets. Ed. by Robert Stafford, ARM user facility. DOE/SC-ARM-TR-245.

41. Atmospheric Radiation Measurement (ARM) user facility. 2014, updated hourly. Microwave Radiometer, 3 Channel (MWR3C). 2014-02-25 to 2021-09-19, Eastern North Atlantic (ENA) Graciosa Island, Azores, Portugal (C1). Compiled by M. Cadeddu, G. Gibler and A. Koontz. ARM Data Center. Data set accessed 2021-09-21 at http://dx.doi.org/10.5439/1025248.
Atmospheric Radiation Measurement (ARM) user facility. 2011, updated hourly. Microwave Radiometer, 3 Channel (MWR3C). 2011-10-01 to 2021-09-19, Southern Great Plains (SGP) Central Facility, Lamont, OK (C1). Compiled by M. Cadeddu, G. Gibler and A. Koontz. ARM Data Center. Data set accessed 2021-09-21 at http://dx.doi.org/10.5439/1025248.
Atmospheric Radiation Measurement (ARM) user facility. 2013, updated hourly. Microwave Radiometer, 3 Channel (MWR3C). 2013-10-01 to 2021-06-15, ARM Mobile Facility (OLI) Oliktok Point, Alaska; AMF3 (M1). Compiled by M. Cadeddu, G. Gibler and A. Koontz. ARM Data Center. Data set accessed 2021-09-21 at http://dx.doi.org/10.5439/1025248.

42. Atmospheric Radiation Measurement (ARM) user facility. 2014, updated hourly. MWR Retrievals with MWRRET Version 2 (MWRRET2TURN). 2014-05-01 to 2020-12-31, Eastern North Atlantic (ENA) Graciosa Island, Azores, Portugal (C1). Compiled by K. Gaustad. ARM Data Center. Data set accessed 2021-09-21 at http://dx.doi.org/10.5439/1566156.
Atmospheric Radiation Measurement (ARM) user facility. 2014, updated hourly. MWR Retrievals with MWRRET Version 2 (MWRRET2TURN). 2014-11-11 to 2019-09-30, ARM Mobile Facility (OLI) Oliktok Point, Alaska; AMF3 (M1). Compiled by K. Gaustad. ARM Data Center. Data set accessed 2021-09-21 at http://dx.doi.org/10.5439/1566156.
Atmospheric Radiation Measurement (ARM) user facility. 2011, updated hourly. MWR Retrievals with MWRRET Version 2 (MWRRET2TURN). 2011-10-01 to 2019-10-31, Southern Great Plains (SGP) Central Facility, Lamont, OK (C1). Compiled by K. Gaustad. ARM Data Center. Data set accessed 2021-09-21 at http://dx.doi.org/10.5439/1566156.

43. Fernandes, M., Nunes, A., & Lázaro, C. (2013). Analysis and Inter-Calibration of Wet Path Delay Datasets to Compute the Wet Tropospheric Correction for CryoSat-2 over Ocean. Remote Sensing, 5(10), 4977–5005. doi:10.3390/rs5104977

44. Thayer, G. D. (1974). An improved equation for the radio refractive index of air. Radio Science, 9(10), 803–807. doi:10.1029/rs009i010p00803

45. Byun, S. H., & Bar-Sever, Y. E. (2009). A new type of troposphere zenith path delay product of the international GNSS service. Journal of Geodesy, 83(3-4), 1–7. doi:10.1007/s00190-008-0288-8

46. Benevides, P., Catalão, J., Miranda, P., & Chinita, M. J. (2013). Analysis of the relation between GPS tropospheric delay and intense precipitation. Remote Sensing of Clouds and the Atmosphere XVIII; and Optics in Atmospheric Propagation and Adaptive Systems XVI. doi:10.1117/12.2028732

47. Zhang, B. (2016). Three methods to retrieve slant total electron content measurements from ground-based GPS receivers and performance assessment. Radio Science, 51(7), 972–988. doi:10.1002/2015rs005916

48. Davis, J. L., Herring, T. A., Shapiro, I. I., Rogers, A. E. E., & Elgered, G. (1985). Geodesy by radio interferometry: Effects of atmospheric modeling errors on estimates of baseline length. Radio Science, 20(6), 1593–1607. doi:10.1029/rs020i006p01593

49. Tregoning, P., & Herring, T. A. (2006). Impact of a priori zenith hydrostatic delay errors on GPS estimates of station heights and zenith total delays. Geophysical Research Letters, 33(23). doi:10.1029/2006gl027706

50. International GNSS Service (IGS). 2021. [Online]. https://www.igs.org/about. Accessed on: 2021/08/19.

51. Kouba, J. (2008). Implementation and testing of the gridded Vienna Mapping Function 1 (VMF1). Journal of Geodesy, 82(4-5), 193–205. doi:10.1007/s00190-007-0170-0

52. Hopfield, H. S. (1969). Two-quartic tropospheric refractivity profile for correcting satellite data. Journal of Geophysical Research, 74(18), 4487–4499. doi:10.1029/jc074i018p04487

53. Boehm, J., Heinkelmann, R., & Schuh, H. (2007). Short Note: A global model of pressure and temperature for geodetic applications. Journal of Geodesy, 81(10), 679–683. doi:10.1007/s00190-007-0135-3

54. Saastamoinen, J. (2013). Atmospheric Correction for the Troposphere and Stratosphere in Radio Ranging Satellites. Geophysical Monograph Series, 247–251. doi:10.1029/gm015p0247

55. Brown, S. (2010). A Novel Near-Land Radiometer Wet Path-Delay Retrieval Algorithm: Application to the Jason-2/OSTM Advanced Microwave Radiometer. IEEE Transactions on Geoscience and Remote Sensing, 48(4), 1986–1992. doi:10.1109/tgrs.2009.2037220

56. Sentinel-6 Michael Freilich. *Copernicus: Sentinel-6 Michael Freilich Mission — formerly Sentinel-6 / Jason-CS (Jason Continuity of Service) Mission*. 2021. [Online]. https://directory.eoportal.org/web/eoportal/satellite-missions/content/-/article/jason-cs. Accessed on: 2021/08/10.

57. Jason-3. *Jason-3 Altimetry Mission*. 2021. [Online]. https://directory.eoportal.org/web/eoportal/satellite-missions/j/jason-3. Accessed on: 2021/08/10.

58. Copernicus: Sentinel-3. *Copernicus: Sentinel-3 — Global Sea/Land Monitoring Mission including Altimetry*. 2021. [Online]. https://directory.eoportal.org/web/eoportal/satellite-missions/c-missions/copernicus-sentinel-3. Accessed on: 2021/08/10.

59. SARAL. *SARAL (Satellite with ARgos and ALtiKa)*. 2021. [Online]. https://directory.eoportal.org/web/eoportal/satellite-missions/s/SARAL. Accessed on: 2021/08/10.

60. Scharroo, R. RADS Version 4.3.7User Manual; 2021.

61. European Centre for Medium-Range Weather Forecasts (ECMWF). 2021. [Online]. https://www.ecmwf.int. Accessed on: 2021/11/01.

62. D. P. Deea, S. M. Uppalaa, A. J. Simmonsa, P. Berrisforda, P. Polia, S. Kobayashi, U. Andraec, M. A. Balmasedaa, G. Balsamoa, P. Bauera, P. Bechtolda, A. C. M. Beljaarsa, L. van de Bergd, J. Bidlota, N. Bormanna, C. Delsola, R. Dragania, M. Fuentesa, A. J. Geera, L. Haimbergere, S. B. Healya, H. Hersbacha, E. V. Ho ́lma, L. Isaksena, P. Ka ̈llbergc,, M. Ko ̈hlera, M. Matricardia, A. P. McNallya, B. M. Monge-Sanzf, J.-J. Morcrettea, B.-K. Parkg, C. Peubeya, P. de Rosnaya, C. Tavolatoe, J.-N. The ́pauta & F. Vitarta. (2011). The ERA-Interim reanalysis: configuration and performance of the data assimilation system. Quarterly Journal of the Royal Meteorological Society, 137(656), 553–597. doi:10.1002/qj.828

63. Yu, C., Li, Z., & Blewitt, G. (2021). Global comparisons of ERA5 andthe operational HRES tropospheric delay and water vapor products with GPS and MODIS. Earth and Space Science, 8, e2020EA001417. https://doi.org/10.1029/2020EA001417

64. Vieira, T., Fernandes, M. J., & Lazaro, C. (2019). Impact of the New ERA5 Reanalysis in the Computation of Radar Altimeter Wet Path Delays. IEEE Transactions on Geoscience and Remote Sensing, 1–9. doi:10.1109/tgrs.2019.2929737

65. Collecte Localisation Satellites (CLS)., 2011. Surface Topography Mission (STM) SRAL/ MWR L2 Algorithms Definition, Accuracy and Specification. Ramonville St-Agne, France. Retrieved from. https://sentinel.esa.int/web/sentinel/user-guides/sentinel- 3-altimetry/document-library/.

66. Bevis, M., Businger, S., Herring, T. A., Rocken, C., Anthes, R. A., & Ware, R. H. (1992). GPS meteorology: Remote sensing of atmospheric water vapor using the global positioning system. Journal of Geophysical Research, 97(D14), 15787. doi:10.1029/92jd01517

67. Bevis, M., Businger, S., Chiswell, S., Herring, T. A., Anthes, R. A., Rocken, C., & Ware, R. H. (1994). GPS Meteorology: Mapping Zenith Wet Delays onto Precipitable Water. Journal of Applied Meteorology, 33(3), 379–386. doi:10.1175/1520-0450(1994)033<0379:gmmzwd>2.0.c

68. Niell, A. E., Coster, A. J., Solheim, F. S., Mendes, V. B., Toor, P. C., Langley, R. B., & Upham, C. A. (2001). Comparison of Measurements of Atmospheric Wet Delay by Radiosonde, Water Vapor Radiometer, GPS, and VLBI. Journal of Atmospheric and Oceanic Technology, 18(6), 830–850. doi:10.1175/1520-0426(2001)018<0830:comoaw>2.0.c

69. Kalakoski, N., Kujanpää, J., Sofieva, V., Tamminen, J., Grossi, M., & Valks, P. (2016). Validation of GOME-2/Metop total column water vapour with ground-based and in situ measurements. Atmospheric Measurement Techniques, 9(4), 1533–1544. doi:10.5194/amt-9-1533-2016

70. Integrated Global Radiosonde Archive (IGRA) [Online]. https://www.ncei.noaa.gov/products/weather-balloon/integrated-global-radiosonde-archive. Accessed on: 2021/10/20.
71. Fernandes, M., & Lázaro, C. (2016). GPD+ Wet Tropospheric Corrections for CryoSat-2 and GFO Altimetry Missions. Remote Sensing, 8(10), 851. doi:10.3390/rs8100851

72. Bosisio, A. V., & Cadeddu, M. P. (2015). Rain detection from ground-based radiometric measurements: Validation against rain sensor observations. 2015 IEEE International Geoscience and Remote Sensing Symposium (IGARSS). doi:10.1109/igarss.2015.73262

73. Vieira, T., Fernandes, & M. J. Lazaro, C. (2021). An enhanced Neural Network-based retrieval of the Wet Tropospheric Correction for Sentinel-3. Manuscript submitted for publication.

74. Obligis, E., Rahmani, A., Eymard, L., Labroue, S., & Bronner, E. (2009). An Improved Retrieval Algorithm for Water Vapor Retrieval: Application to the Envisat Microwave Radiometer. IEEE Transactions on Geoscience and Remote Sensing, 47(9), 3057–3064. doi:10.1109/tgrs.2009.2020433

75. Thao, S., Eymard, L., Obligis, E., & Picard, B. (2015). Comparison of Regression Algorithms for the Retrieval of the Wet Tropospheric Path. IEEE Journal of Selected Topics in Applied Earth Observations and Remote Sensing, 8(9), 4302–4314. doi:10.1109/jstars.2015.2442416

76. Huang, L., Mo, Z., Liu, L., Zeng, Z., Chen, J., Xiong, S., & He, H. (2021). Evaluation of hourly PWV products derived from ERA5 and MERRA-2 over the Tibetan Plateau using ground- based GNSS observations by two enhanced models. Earth and Space Science, 8, e2020EA001516. https://doi. org/10.1029/2020EA001516

77. Picard, B., Frery, M.-L., Obligis, E., Eymard, L., Steunou, N., & Picot, N. (2015). SARAL/AltiKa Wet Tropospheric Correction: In-Flight Calibration, Retrieval Strategies and Performances. Marine Geodesy, 38(sup1), 277–296. doi:10.1080/01490419.2015.1040903

78. University of Alaska Fairkanks | Alaska Center for Climate Assesment and Policy. HISTORICAL SEA ICE ATLAS for ALASKA & the ARCTIC - 1850 to present. [Online]. https://www.snap.uaf.edu/tools/sea-ice-atlas. Accessed on: 2021/10/20.

79. Fernandes, M., & Lázaro, C. (2018). Independent Assessment of Sentinel-3A Wet Tropospheric Correction over the Open and Coastal Ocean. Remote Sensing, 10(3), 484. doi:10.3390/rs10030484